eng

MDPI

Article

Optimisation of Elemental Transfer Efficiency in Fe-C-Cr-Ti-Cu Hardfacing by Self-Shielded Flux-Cored Wire: A Synergistic Taguchi–ANOVA–FD–PCA–GRA Approach

Bohdan Trembach [1,*], Michal Krbata [2], Borys Haibadulov [3], Oleksandr Iokhov [4], Ivan Tsebriuk [5], Ihor Pomohaiev [3], Yurii Korobkov [3] and Larysa Neduzha [6]

[1] Chief Designer Department of Mining and Press-and-Forging Equipment, Private Joint Stock Company "Novokramatorsky Mashinostroitelny Zavod", 04070 Kyiv, Ukraine
[2] Faculty of Special Technology, Alexander Dubcek University of Trenčín, 911 06 Trenčín, Slovakia; michal.krbata@tnuni.sk
[3] Department of Anti-Aircraft Missile Forces Armament, Ivan Kozhedub Kharkiv National Air Force University, 61023 Kharkiv, Ukraine
[4] Simulation Modeling Center, National Academy of the National Guard of Ukraine, 61000 Kharkiv, Ukraine
[5] Department of Armored Vehicles, National Academy of the National Guard of Ukraine, 61000 Kharkiv, Ukraine
[6] Department of Technical Mechanics, Ukrainian State University of Science and Technologies, Lazaryan 2, 49010 Dnipro, Ukraine; nlorhen@i.ua
* Correspondence: btrembach89@gmail.com; Tel.: +380-99-450-0811

Abstract

The objective of this article is to optimise the deposition modes and the content of exothermic additions (*EAs*) in the core filler in Fe-C-Cr-Ti with Cu additions hardfacing. To achieve this, JMatPro Release 7.0, Sente Software Ltd., 2016 material characterisation software was used to simulate and calculate the equilibrium phase structure and composition of the Fe-C-Cr-Ti-Cu alloy during the welding thermal cycle. A synergistic approach combining the Taguchi–Analysis of Variance (ANOVA)–Factorial design (FD) method with the standard hybrid Taguchi–ANOVA–Principal Component Analysis (PCA)–Grey Relational Analysis (GRA) is used and justified to optimise factors and develop mathematical models for parameters in the L9 orthogonal experimental design. The study examines how the transfers of deoxidisers depend on the content of exothermic additions in the cored wire filler (*EA*) and the contact tip-to-work distance (*CTWD*), while the behaviour of carbide formers is influenced by wire feed speed (*WFS*) and present arc voltage at the power source (U_{set}). The research specifically investigates the Fe-C-Cr-Ti-Cu system and the role of copper in stabilising austenite. Findings show that high Cu concentrations (7 wt.%) enhance hardenability by 13%, effectively suppressing pearlite transformation and expanding the bainite region. The desired chemical composition of the deposited metal is determined by the distribution of selected factors, as measured by the transfer coefficients of each element.

Keywords: flux-cored arc welding; exothermic addition; CuO-Al; Fe-C-Cr-Ti-Cu; copper alloying; element transfer coefficient; element recovery factors; hardfacing; PCA; GRA

Academic Editors: Kai Wang, Jingmang Xu and Yao Qian

Received: 2 February 2026
Revised: 8 March 2026
Accepted: 17 March 2026
Published: 20 March 2026

1. Introduction

In 2024, the global market volume of welding products was estimated to exceed USD 15 billion [1,2]. Welding consumables and technologies are a key driver of global growth in the welding market [3,4]. These technologies play a significant role in numerous industrial

sectors, including the chemical industry, construction [5], the oil and gas industry, railway engineering [6–8], and automotive manufacturing [9,10]. Surfacing processes are widely used for both surface hardening and the restoration of worn components [11]. In the former case, cost reduction is achieved by using inexpensive, technologically advanced substrate materials such as structural steels [12,13]. In the latter case, the service life of components is extended. This is done through localised restoration of worn geometries. At the same time, high wear resistance is ensured [14]. In engineering practice, several surface strengthening technologies are employed. These include processes in the solution state, such as sol–gel, electrochemical deposition, and chemical solution deposition [15]; the gaseous state, such as ion beam-assisted deposition (IBAD), chemical vapour deposition (CVD), and physical vapour deposition (PVD) [16]; and the molten or semi-molten state, such as arc welding [17,18], plasma technologies [19–22], thermal spraying [23–25], and laser or electron beam processing [26–28]. However, hardfacing processes remain the most widely used due to their cost-effectiveness, technological simplicity, and broad industrial accessibility [29]. Using hardfacing technologies significantly reduces the cost of final products by enabling the use of large components made from inexpensive structural materials. Meanwhile, surface layers with enhanced tribological properties are formed only in zones subject to severe operating conditions. The most commonly used arc hardfacing techniques include shielded metal arc welding (SMAW) [30,31], gas tungsten arc welding (GTAW [32–34] or TIG [35,36]), gas metal arc welding (GMAW) [37–40], submerged arc welding (SAW) [41–44], manual metal arc welding (MMAW) [45,46], and flux-cored arc welding (FCAW) [47–51]. In recent decades, self-shielded flux-cored arc welding (FCAW-S) has gained prevalence in industry due to its high productivity, technological flexibility, and ability to produce hardfacing layers with customisable operational properties [52–57]. This approach effectively resists various types of wear [58], including abrasive [59,60], corrosive [61–63], impact-abrasive [64,65], abrasive-corrosive [66,67], and thermal softening [11]. Shape retention of wear-resistant parts allowed to preserve the performance and reliability of machine units [68–70], reduce dynamic stresses [71–73], and increase the operational lifespan of facilities and structures [74,75]

The properties of the deposited metal are determined by the chemical composition of the hardfacing layer. This layer is formed as a result of complex physicochemical processes occurring in the welding arc, the molten pool and during metal solidification [76,77]. The deposition conditions, which define the welding thermal cycle, also play a crucial role [78–80]. Carbide-forming elements are commonly used as primary alloying elements. These include chromium [81,82], titanium [83,84], vanadium [85], tungsten [86], and boron [87–89], among others. These elements form hard phases in the microstructure of the deposited metal in the form of carbides, carbonitrides, carboborides, and similar compounds. The transition of alloying elements from the powdered filler and the metallic sheath of the wire into the deposited metal is of particular importance [90–93].

Self-shielded flux-cored wires are complex multicomponent systems due to the presence of slag-forming, gas-forming, and deoxidising components in their composition, which significantly complicates the kinetics of the involved reactions [2,94]. The hardfacing process consists of two main stages: the formation of a molten metal droplet and a flux column, followed by the transfer of electrode material into the weld pool [95]. In the first stage, a molten metal droplet forms alongside the development of a flux column, which is a protrusion of the filler material [96–98]. In the second stage, the molten metal droplet is transferred into the weld pool. Depending on the hardfacing parameters (welding current, arc voltage, and contact tip-to-work distance) and the characteristics of the flux-cored wire (wire design, filler composition, and filling coefficient [98–101]), the molten metal droplet may form in one of two sub-modes (Figure 1): Type A (asymmetric) and Type B (central).

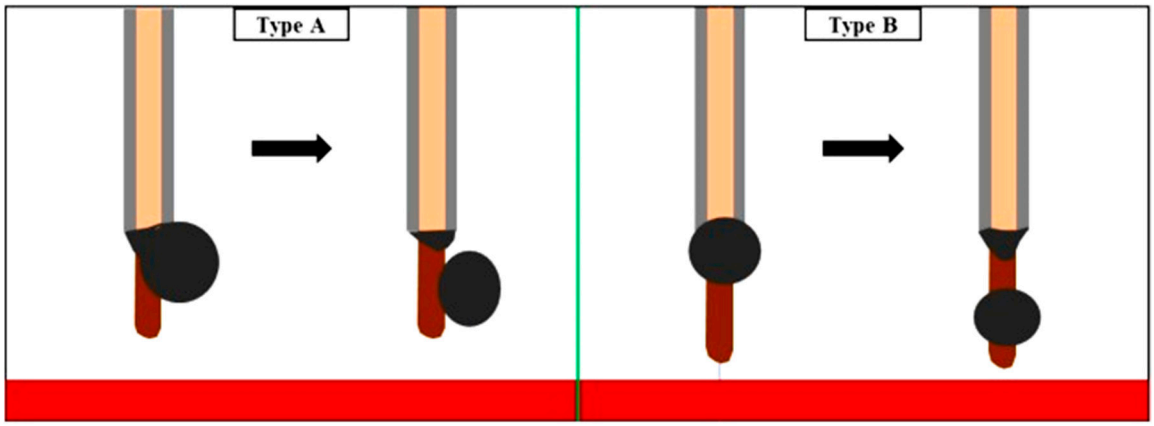

Figure 1. Classification of two sub-modes in projected transfer mode [98].

Upon forming, the flux column may either melt and mix with the molten metal droplet or collapse into the weld pool when it reaches a critical length or mass [92,95]. The melting of the flux column is caused by heat transfer from direct contact with the molten droplet (liquid metal of the wire sheath), Joule heating, as well as convective heat from the arc and the weld pool. This accounts for up to 15–30% of the total core filler volume [95]. On the other hand, flux column collapse is linked to forces like arc pressure and plasma shear forces. In these conditions, the flux column often separates from the metallic part several milliseconds before the metal droplets [98]. Large agglomerates subsequently fall onto the surface of the weld pool and are displaced by convective and gas-dynamic flows towards the trailing, crystallising region of the pool. There is insufficient time for them to dissolve in the liquid alloy [102]. Consequently, alloying elements from the flux-cored wire filler are transferred into the deposited metal via two pathways: through the molten metal droplet or through fragments of the flux column entering the weld pool directly. According to [102], the former mechanism is preferable as it results in a higher proportion of the alloying elements being dissolved by diffusion in the molten metal. The transfer of elements at the droplet stage can be described by the interaction between the molten metal and an annular layer of the charge with a thickness Δ, located adjacent to the wire sheath (Figure 2). This is based on the effective layer model proposed by Erokhin et al. [90]. The completeness of this interaction is characterised by the element transfer coefficient, which depends mathematically on the inner wire radius r_1 and the current density j. It has been established that an increase in current density leads to a systematic decrease in the effective layer thickness, Δ. Thus, the formation of a flux column during non-uniform electrode melting has a detrimental effect on the transfer of elements from the flux-cored wire filler into the deposited metal. It also contributes to the contamination of the hardfacing layer with non-metallic inclusions.

The most important challenges in modern welding technologies are the use of materials and processes that save energy, reducing and recycling waste, and optimising resources. The focus here is particularly on the environmental benefits and economic efficiency of the process [56,103]. Incorporating exothermic additions into the filler of flux-cored wires has been shown to enhance the energy efficiency and productivity of hardfacing processes [104–106], reduce droplet size [107] and improve the quality of the deposited metal [108–112]. However, the presence of an exothermic addition can significantly impact the uniformity of melting of both the metallic sheath and the flux-cored wire filler [92]. Depending on the hardfacing parameters and the thermophysical properties of the exothermic addition, the exothermic reaction may occur in one of two regions of the process: (1) in the electrode extension section due to Joule heating [113], or (2) within the arc column and flux column under the influence of arc heat [114,115] (see Figure 3).

In the first case, introducing the exothermic addition results in uniform melting of both the core filler and the metallic sheath. In the second case, the intense heat released by the exothermic reaction can cause significant overheating of the droplets during transfer or neck rupture during short-circuit transfer [115]. This can substantially affect the behaviour of conventional metal droplet transfer.

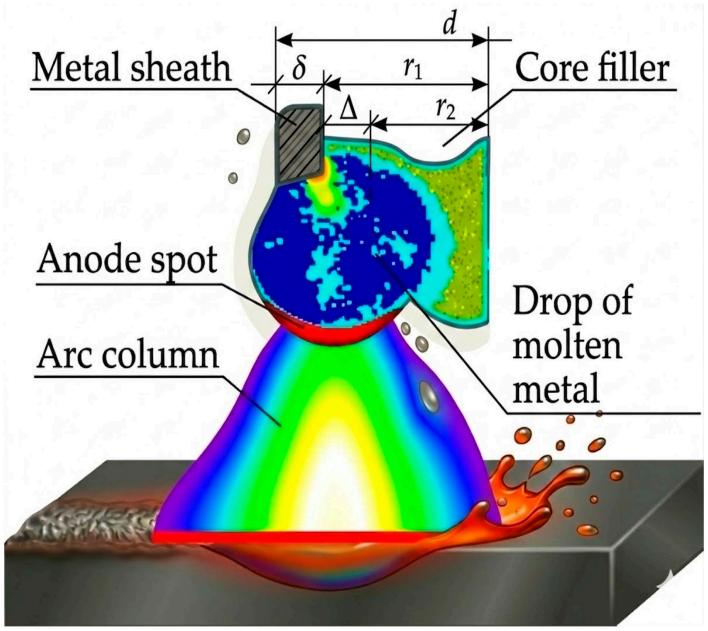

Figure 2. Schematic diagram showing the transition of filler material (thickness Δ) passing into a drop of molten material located asymmetrically at the end of a metal shell. The shell is made of powder wire with a thickness δ and a diameter *d* [90].

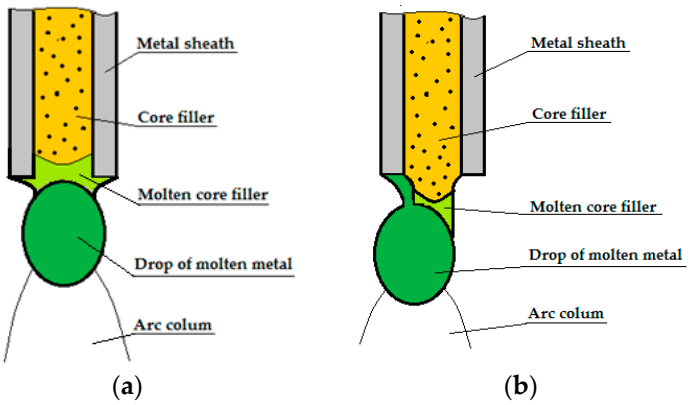

Figure 3. Classification of stages of exothermic reactions: (**a**) electrode extension section; (**b**) flux column.

In the first case, the metallic sheath and the core filler melt uniformly; however, the deposited metal may become more susceptible to atmospheric contamination due to the premature decomposition of gas-forming components. In the second case, the filler material may become excessively overheated due to intense additional chemical heat release. This can result in metal expulsion. This, in turn, contributes to increased burn-off losses and spattering. Trembach et al. [115] investigated the influence of the amount of *EA* introduced into the flux-cored wire filler and the hardfacing parameters on melting characteristics and weld bead morphology. As shown in Table 1, the deposition rate was found to be most influenced by the wire feed speed, in combination with the amount of exothermic addition. Conversely, the spattering factor and deposition efficiency were primarily affected

by the exothermic addition content and the contact tip-to-work distance. This indicated a significant contribution of the chemical reaction to the overall energy balance during the melting of flux-cored wire.

Table 1. Melting characteristics [115].

№ Exp	Melt-off Rate *MOR*, [kg·hr^{-1}]	Deposition Rate *DR*, [kg·hr^{-1}]	Spattering Factor *SF* [%]	Deposition Efficiency *De* [%]
1	4.43	3.88	9.68	87.55%
2	4.83	4.28	8.45	88.70%
3	5.04	4.52	10.12	89.68%
4	5.38	4.79	10.15	89.09%
5	5.73	5.07	11.12	88.53%
6	4.85	4.51	6.02	93.02%
7	5.52	5.16	5.35	93.54%
8	4.37	3.98	7.9	91.00%
9	5.04	4.83	3.52	95.76%

Investigating the transition of elements from core-filler materials into the deposited metal is still a challenging area of investigation. Without a clear understanding of the mechanisms influencing the behaviour of elements during hardfacing and their assimilation by the deposited metal, it is not possible to select the composition of flux-cored wire rationally. Therefore, studying element transition during hardfacing with self-shielded flux-cored wires is important from both scientific and technological perspectives. There are no published studies investigating the influence of surfacing conditions on the uptake of alloying elements by the deposited metal when surfacing with flux-cored wires containing an exothermic CuO-Al core filler. Research on the effect of reduced copper from *EA* on the microstructure, phase composition, and mechanical properties of deposited metal in the Fe-Cr-Ti-Cu system is also limited. The present work has two aims. First, it aims to conduct a comprehensive investigation into the element transition characteristics during hardfacing with self-shielded flux-cored wires. Secondly, the influence of technological parameters on the chemical composition and properties of the deposited metal is to be investigated.

2. Materials and Methods

2.1. Statistical Evaluation

The experimental methodology employed in this study was based on the approach described in references [110,115]. This combined approach [116–118] and standard hybrid method [119–121] were applied to an orthogonal four-factor, three-level experimental design. The combined approach identifies the most significant factors and eliminates insignificant variables through ANOVA. A factorial experimental design can be used to develop mathematical models that describe the target-dependent variables. In contrast, the hybrid Taguchi–Principal Component Analysis (PCA)–Grey Relational Analysis (GRA) method is employed to optimise the variables under investigation in processes characterised by multiple interdependent quality responses. PCA reduces data dimensionality by transforming correlated response variables into a smaller set of uncorrelated principal components while preserving dominant sources of variability [122,123].

2.1.1. Taguchi's Design of Experiment

As the main experimental design, an orthogonal array based on the Taguchi method was employed. Four factors were investigated: the *EA*, *CTWD*, *WFS*, and U_{set}. The values of each variable were selected based on preliminary tests, conducted to establish the optimal valuesfor the variables. The *EA* content was varied at three levels of 20, 30, and 40 wt.%,

while the *CTWD* was set to 35, 40, and 45 mm. The wire feed speed was adjusted to 1.50, 2.07, and 2.73 m·min^{-1}, and the set voltage values were 28, 31, and 34 V. The selection of experimental ranges was fundamentally grounded in the thermodynamic behaviour of self-shielding flux-cored wires with exothermic additions (*EA*). The *EA* content (20–40 wt.%) was optimised to balance internal chemical heat generation with the stability of the gas-slag protection [107,112,114], while the increased *CTWD* (35–45 mm) was specifically chosen to utilise Joule–Lenz heating. According to the calculation methodology proposed by Kassov et al. [124], this increased distance ensures sufficient preheating of the core to initiate the exothermic reaction before the arc zone [114]. The ranges for wire feed speed (1.50–2.73 m·min^{-1}) and arc voltage (28–34 V) were further refined to maintain a stable metal transfer mode, ensuring that the rate of the internal core reaction harmonises with the melting rate of the metallic sheath to prevent porosity and excessive spatter [104,108,110]. The nine experiments were conducted according to Table 2, and each experiment was repeated three times.

Table 2. Design matrix of the experiment of full factor analysis using the orthogonal array L9 by the method.

№ Exp.	Fact Mean			
	***EA*, [wt.%]**	***CTWD*, [mm]**	***WFS*, [m·min^{-1}]**	**U_{set}, [V]**
1	18	35	1.63	28
2	18	40	1.85	31
3	18	45	2.07	34
4	28	35	1.85	34
5	28	40	2.07	28
6	28	45	1.63	31
7	38	35	2.07	31
8	38	40	1.63	34
9	38	45	1.85	28

The content of the exothermic addition and the parameter variables of the hardfacing modes were optimised using the STATISTICA software Version 6.0 (Statsoft Inc., Tulsa, OK, USA, 2006).

2.1.2. Grey Relational Analysis

To facilitate the GRA process, raw data were normalised to calculate both the GRC and GRG values. Initially, a grey relational matrix was established by scaling the performance metrics to a normalised interval [0, 1]. This systematic approach was implemented for each of the three quality criteria. In accordance with the methodologies suggested by previous studies [115,123], the specific performance indicators summarised in Table 2 were evaluated using the following mathematical expressions [115,123]:

$$X_i^* = \frac{X_{i\max} - X_i}{X_{i\max} - X_i\min} \text{ (smaller is better)}, \quad (1)$$

$$X_i^* = \frac{X_i - X_{i\min}}{X_{i\max} - X_i\min} \text{ (larger is better)}, \quad (2)$$

where $i = 1, \ldots, m$ and $k = 1, \ldots, n$; $m = 9$ is the number of experimental runs and $n = 4$ is the number of process factors. The term X_i^0 represents the original or reference sequence; X_i^0min and X_i^0max represents the minimum and maximum values in the original sequence; X_i^* represents the sequence produced after data processing.

The GRC after data processing was calculated with the particular deviation calculations as given in Equations (3) and (4) [115,123]:

$$\Delta_{oi}(k) = |X_i^* - X_i|, \tag{3}$$

$$\xi_i(k) = \frac{\Delta_{\min} + \psi \cdot \Delta_{\max}}{\Delta_{oi}(k) + \psi \cdot \Delta_{\max}}, \tag{4}$$

where $\Delta_{oi}(k)$ is the deviation sequence of the original reference sequence of X_i^* and compatibility sequence X_i; ψ is the distinguishing coefficient and is usually taken as 0.5 when equal weightage is given to the process parameters.

Evaluated on a scale between 0 and 1, the GRG serves as a quantitative measure of the relational proximity between the reference and comparative sequences. Elevated GRG values reflect a stronger correspondence among the integrated process factors, which designates the most favourable operating conditions [115,123]:

$$\gamma_i(GRC) = \frac{1}{n}\sum_{k=1}^{n} \xi_i(k), \tag{5}$$

where $\gamma_i(GRG)$ is the i-th experiment and n represents the number of performance characteristics.

The higher value of the grey relational grade shows that the corresponding experimental results are closer to the optimum value or normalised value.

2.1.3. Principal Component Analysis

To analyse the variance and covariance of the investigated performance parameters, Principal Component Analysis (PCA) [76] was utilised. This method facilitates the linear integration of variables to identify underlying patterns in the dataset. In accordance with the frameworks described by [115,123], the computational phases of the PCA approach are structured as follows [115,123]:

$$X_i = \begin{matrix} X_1(1) & X_1(2) & \dots & X_1(n) \\ X_2(1) & X_1(2) & \dots & X_1(n) \\ \dots & \dots & \dots & \dots. \\ X_m(1) & X_1(2) & \dots & Xm_1(n) \end{matrix}, \tag{6}$$

where $X_i(j)$, i = 1 to m, j = 1 to n. Here in this study, X represents the GRC of each performance characteristic.

The computation of the correlation coefficient array is computed using the following equation [115,123]:

$$R_i(k) = \left(\frac{\mathrm{cov}(X_i(j), X_i(\updownarrow))}{\sigma_{Xi}(j) \cdot \sigma_{Xi}(\updownarrow)}\right), \tag{7}$$

where $\mathrm{cov}(X_i(j), X_i(\updownarrow))$ is the covariance sequence of $X_i(j)$ and $X_i(\updownarrow)$, and $\sigma_{Xi}(j)$, $\sigma_{Xi}(\updownarrow)$ are the standard deviations of the sequence $X_i(j)$ and $X_i(\updownarrow)$ respectively.

Then, the eigenvectors and eigenvalues are determined by using a coefficient correlation array with the help of the equation shown below [115,123]:

$$(R_i(k) - \lambda_k \cdot \updownarrow) \cdot v_k = 0, \tag{8}$$

Where $R_i(k)$ is the correlation coefficient matrix form $R_i(k)$, λ_k is the k-th eigenvalue, $\sum_{k=1}^{n} \lambda_k = n$, k = 1, 2. . ., n and $V_{i,k}$ = [$ak1$, $ak2$, . . ., akn] is the eigenvector corresponding to the eigenvalue λ_k.

The principal component of each response value can be determined as follows [115,123]:

$$Y_{mk} = \sum_{i=1}^{n} X_m(i) \cdot v_{ik}. \quad (9)$$

The grey relational grade for each response can be calculated using the following equation [123]:

$$\gamma_i(GRC) = \frac{1}{n} \sum_{k=1}^{n} \xi_i(k). \quad (10)$$

2.2. Filler Materials

For this study, three self-shielded flux-cored wire specimens with a diameter of 4 mm were manufactured. The fabrication process involved multiple drawing passes through calibrated dies with a gradual reduction in the outlet diameter. A low-carbon steel strip made of St 24 steel (DIN 1614.1) in the annealed condition was used as the material for the metal sheath, with dimensions of 20 mm in width and 0.5 mm in thickness.

The main filler consisted of gas- and slag-forming components (fluorite, rutile, and calcium carbonate, at 12%, 7%, and 4% by weight, respectively), which protected the molten metal from atmospheric contamination and aided its purification. In addition, alloying, deoxidisers elements and *EA* components were incorporated into the filler to control chemical composition and enhance process efficiency. The exothermic addition was prepared with the following composition: Graphite (4.5 wt.%); Metallic chromium (14.5 wt.%); Ferromanganese (6 wt.%); Ferrosilicon (4 wt.%); Ferrovanadium (4 wt.%); Titanium powder (5 wt.%); Iron powder (balance). The detailed composition of the exothermic additive is presented in Table 3. The oxidiser-to-reductant ratio was selected according to stoichiometric proportions. The coefficients of wire filling (C_{WF}) for the experimental flux-cored wires were 0.342, 0.345 and 0.348.

Table 3. Composition of core filler FCAW-SS, wt.%.

The Name of the Component	Content of the Components in Core Filler of FCAW-S, [wt.%]		
	FCAW-P3-E1-1	**FCAW-P3-E1-2**	**FCAW-P3-E1-3**
Oxide of copper powder GOST 16539-79	15	23.3	32.5
Aluminium powder PA1 GOST 6058-73	3	4.7	6.5

2.3. Hardfacing Procedure

The hardfacing was applied to the steel plates using the single-pass roller method. These plates were made of low-carbon steel (S235J2+N steel, manufactured in accordance with EN 10025-2 were sourced from the Azovstal Iron and Steel Works, Mariupol, Ukraine) measuring 10 × 100 × 200 mm. The hardfacing process was conducted using an A-874 automatic welding system (Paton Electric Welding Institute, Kyiv, Ukraine). This unit, designed for mechanised arc welding and hardfacing, provided precise control over electrode wire feed (2.0–5.0 mm) and travel speeds (15–120 m/h). This was equipped with a power source featuring a rigid volt-ampere characteristic under reverse polarity. The travel speed was set to *TS* = 18 m/h and remained constant throughout. The selection of the travel speed parameter was made based on experience. It was also based on preliminary research [108].

2.4. Calculation of the Elements' Transfer Coefficients and the Recovery Coefficient

In this case, the element transfer coefficient ($\eta(E)$) and element recovery factor ($RF(E)$) of the alloying elements determine the outcome of the individual reactions that occur at various stages of filler material melting and weld pool formation [92].

The assimilation coefficients of the *i*-th element *TF*(*E*) and the element recovery coefficients (*RF*) were calculated using improved equations that account for losses of filler metal, deposition efficiency, and spatter losses [91,92]:

$$\eta(E) = \frac{Me_d \cdot De}{C_{WF} \cdot K_{WF} \cdot (100 - SF)}, \quad (11)$$

$$RF(E) = \frac{Me_d \cdot De}{C_{WF} \cdot K_{WF} \cdot (100 - SF)}, \quad (12)$$

where Me_d is the content of alloying element in deposited metal, wt.%; C_{WF} is the coefficient wire filling of the FCAW-S; K_{WF} is the concentration of component in the flux core FCAW–S, wt.%; $K(E)$ is the concentration of alloying element in the content of component of the core filler, wt.%; *De* is deposition efficiency, %; *SF* is spattering factor, %.

The total transition coefficient of alloying elements ($\eta(SS)$) was determined. The method used was as follows [91]:

$$\eta(SS) = \sum_{1}^{p} (\eta(E) \cdot C_o) + \sum_{1}^{o} (RF(E) \cdot C_o), \quad (13)$$

where C_i, C_j are the corresponding proportions of the components in the filler *p*, and the *o* are components of the oxides that are reduced.

3. Results

3.1. Elemental Composition of the Deposited Metal

Chemical composition analysis of the experimental FCAW–S weld metal was performed using a Spectrolab LAVFC01A optical emission spectrometer (SPECTRO Analytical Instruments GmbH, Kleve, Germany). The findings of this investigation are presented in Table 4.

Table 4. Chemical composition of samples of applied metal steel of the Fe-C-Cr-Ti-Cu system in three layers.

Item No.	Content of Alloying Element in Metal Deposit, wt.%										
	C	**Cr**	**Cu**	**Si**	**Mn**	**Ti**	**V**	**Al**	**N**	**P**	**S**
P3-E1-1	0.51	2.49	3.1	0.79	1.08	0.43	0.39	0.23	0.042	0.022	0.024
P3-E1-2	0.58	3.06	3.4	0.69	1.28	0.4	0.43	0.25	0.043	0.021	0.024
P3-E1-3	0.61	2.76	3.4	0.72	1.18	0.45	0.43	0.27	0.043	0.019	0.021
P3-E1-4	0.71	3.9	5.7	1.05	1.88	0.72	0.37	0.17	0.044	0.022	0.024
P3-E1-5	0.86	4.04	6.05	1.01	1.98	0.61	0.37	0.19	0.043	0.022	0.024
P3-E1-6	0.57	3.55	6.7	1.04	1.79	0.83	0.3	0.24	0.045	0.017	0.019
P3-E1-7	0.5	2.36	7.5	1.15	1.41	0.61	0.22	0.28	0.045	0.017	0.019
P3-E1-8	0.52	2.7	8.6	1.13	1.71	0.83	0.26	0.25	0.043	0.018	0.020
P3-E1-9	0.77	3.1	6.8	1	1.82	0.59	0.34	0.39	0.044	0.018	0.019

The chemical composition of the investigated alloys varied within the following ranges: C = 0.50–0.86 wt.%, Mn = 1.04–1.88 wt.%, Cr = 2.49–4.04 wt.% and Cu = 3.1–8.8 wt.%. In addition, minor alloying additions of V and Ti were present. The results showed that the copper content of the deposited metal clearly depended on the total amount of exothermic addition introduced into the core filler of the flux-cored wire. The deposited metal samples produced using FCAW-S with filler material P3-E1-1 (samples P3-E1-1, P3-E1-2 and P3-E1-3) contained a relatively low and stable copper content of 3.1–3.4 wt.%. By contrast, the deposited metal obtained using P3-E1-2 filler material exhibited a wider

copper concentration range of 5.7–6.7 wt.%. The greatest variation in copper content was observed in deposits produced using filler materials containing the highest proportion of *EA* (40 wt.% of the core filler), which corresponded to P3-E1-3. In this case, the copper content ranged from 6.8 to 7.5 wt.%, which indicates that copper transfer is more sensitive to the content of the exothermic addition in the wire.

3.2. Element Transfer Coefficient

3.2.1. Experiment Results for Element Transfer Coefficient

The results obtained for the element transition coefficients for each experiment are shown in Table 5. The results obtained for the copper recovery factor for each experiment are shown in Table 6.

Table 5. Experimental and calculated values of the element transfer coefficient.

№ Exp.	Carbon Transfer Coefficient				Chrome Transfer Coefficient			
	$\eta(C)(e)$	$\eta(C)(c)$	Difference	Deviation	$\eta(Cr)(e)$	$\eta(Cr)(c)$	Difference	Deviation
1	0.375	0.411	−0.036	9.7%	0.638	0.664	−0.026	4.1%
2	0.433	0.483	−0.050	11.5%	0.785	0.739	0.047	5.9%
3	0.443	0.432	0.011	2.5%	0.686	0.707	−0.020	2.9%
4	0.532	0.501	0.031	5.8%	0.955	0.989	−0.035	3.7%
5	0.653	0.636	0.017	2.7%	0.989	0.976	0.013	1.4%
6	0.410	0.331	0.079	19.2%	0.850	0.829	0.021	2.5%
7	0.365	0.393	−0.029	7.9%	0.728	0.731	−0.003	0.4%
8	0.370	0.413	−0.042	11.4%	0.809	0.815	−0.006	0.7%
9	0.561	0.542	0.019	3.4%	0.918	0.909	0.008	0.9%
min	0.375				0.638			
max	0.653				0.989			
№ Exp.	**Titanium Transfer Coefficient**				**Vanadium Transfer Coefficient**			
	$\eta(Ti)(e)$	$\eta(Ti)(c)$	Difference	Deviation	$\eta(V)(e)$	$\eta(V)(c)$	Difference	Deviation
1	0.358	0.363	−0.005	1.5%	0.797	0.848	−0.051	6.4%
2	0.333	0.352	−0.018	5.5%	0.880	0.843	0.037	4.2%
3	0.364	0.340	0.024	6.5%	0.853	0.839	0.014	1.7%
4	0.592	0.587	0.005	0.8%	0.747	0.672	0.075	10.0%
5	0.502	0.533	−0.032	6.3%	0.747	0.736	0.011	1.5%
6	0.668	0.641	0.027	4.0%	0.593	0.679	−0.086	14.6%
7	0.506	0.452	0.054	10.6%	0.597	0.742	−0.145	24.2%
8	0.669	0.644	0.025	3.7%	0.686	0.683	0.003	0.5%
9	0.470	0.548	−0.078	16.7%	0.886	0.744	0.141	16.0%
min	0.333				0.672			
max	0.669				0.848			
№ Exp.	**Silicon Transfer Coefficient**				**Manganese Transfer Coefficient**			
	$\eta(Si)(e)$	$\eta(Si)(c)$	Difference	Deviation	$\eta(Mn)(e)$	$\eta(Mn)(c)$	Difference	Deviation
1	0.728	0.710	0.017	2.4%	0.575	0.583	−0.008	1.3%
2	0.630	0.665	−0.035	5.6%	0.699	0.684	0.015	2.2%
3	0.639	0.622	0.017	2.7%	0.618	0.625	−0.008	1.2%
4	0.973	0.966	0.007	0.7%	0.902	0.904	−0.002	0.2%
5	0.934	0.949	−0.015	1.6%	0.954	0.951	0.003	0.4%
6	0.942	0.935	0.007	0.8%	0.837	0.839	−0.002	0.2%
7	0.959	0.972	−0.014	1.4%	0.773	0.763	0.009	1.2%
8	0.915	0.887	0.027	3.0%	0.929	0.948	−0.019	2.0%
9	0.794	0.808	−0.014	1.7%	0.982	0.973	0.009	0.9%
min	0.630				0.575			
max	0.973				0.982			

Table 5. *Cont.*

№ Exp.	Aluminium Transfer Coefficient				Total Element Transition Coefficient			
	$\eta(Al)(e)$	$\eta(Al)(c)$	Difference	Deviation	$\eta(SS)(e)$	$\eta(SS)(c)$	Difference	Deviation
1	0.211	0.214	−0.002	1.0%	0.449	0.453	−0.004	0.9%
2	0.230	0.218	0.012	5.2%	0.503	0.506	−0.003	0.5%
3	0.241	0.251	−0.010	4.1%	0.475	0.469	0.007	1.4%
4	0.103	0.106	−0.003	3.1%	0.705	0.693	0.012	1.6%
5	0.115	0.111	0.004	3.8%	0.734	0.746	−0.013	1.7%
6	0.142	0.143	−0.001	0.8%	0.710	0.709	0.001	0.1%
7	0.128	0.123	0.005	4.1%	0.683	0.690	−0.008	1.1%
8	0.111	0.128	−0.016	14.7%	0.759	0.743	0.015	2.0%
9	0.171	0.160	0.011	6.5%	0.698	0.706	−0.008	1.1%
min	0.103				0.449			
max	0.241				0.759			

Table 6. Experimental and calculated values of the recovery factor.

№ Exp.	Copper Recovery Coefficient			
	$RE(Cu)(e)$	$RE(Cu)(c)$	Difference	Deviation
1	0.713	0.704	0.009	1.3%
2	0.783	0.805	−0.022	2.8%
3	0.759	0.746	0.013	1.7%
4	0.863	0.874	−0.011	1.3%
5	0.916	0.919	−0.003	0.3%
6	0.993	0.979	0.014	1.4%
7	0.859	0.850	0.008	1.0%
8	0.957	0.959	−0.002	0.2%
9	0.747	0.753	−0.006	0.8%
min	0.713			
max	0.993			

The indices on the right side of the geometric parameter notation have the following meanings: (e)—experimental values; (c)—calculated values obtained by introducing the corresponding values of variables into the developed mathematical models.

3.2.2. Taguchi Method and ANOVA for Element Transfer Coefficient

The Taguchi method was used to obtain the experimental results for parameters of element transfer coefficient, as shown in Figure 4.

ANOVA was applied to determine the percentage contribution of the welding parameters to the melting characteristics. The results are presented in Figure 5.

The analysis revealed that the investigated variables had a similar influence on the transition coefficients of carbon and vanadium. Figure 5a1,a2 show that three variables had a significant impact on the transition coefficients of carbon and transition coefficients vanadium *EA*, *WFS*, and U_{set}. The influence of the *CTWD* was found to be within the noise level and therefore negligible. The optimal conditions for achieving maximum values of $\eta(C)$ and $\eta(V)$ were identified as WFS = 1.85 m·min^{-1} and U_{set} = 28 V (Figure 4c,f). The optimal *EA* content value differed for these elements and was located at low to medium levels (Figure 4c,f). Figure 5 also shows that the *EA* had a significant effect on the $\eta(SS)$ (Figure 4b). Figure 5a1 show a similar response of $\eta(Al)$, $\eta(Si)$, and $\eta(Mn)$ to the variables under investigation. These elements acted as active deoxidisers and were strongly affected by the *CTWD*. The optimal exothermic addition content for aluminium, silicon, and manganese transitions was identified as *EA* = 30 wt.% (see Figure 4b,g,h), whereas the optimal *CTWD* corresponded to *CTWD* = 35 mm (see Figure 4b,g).

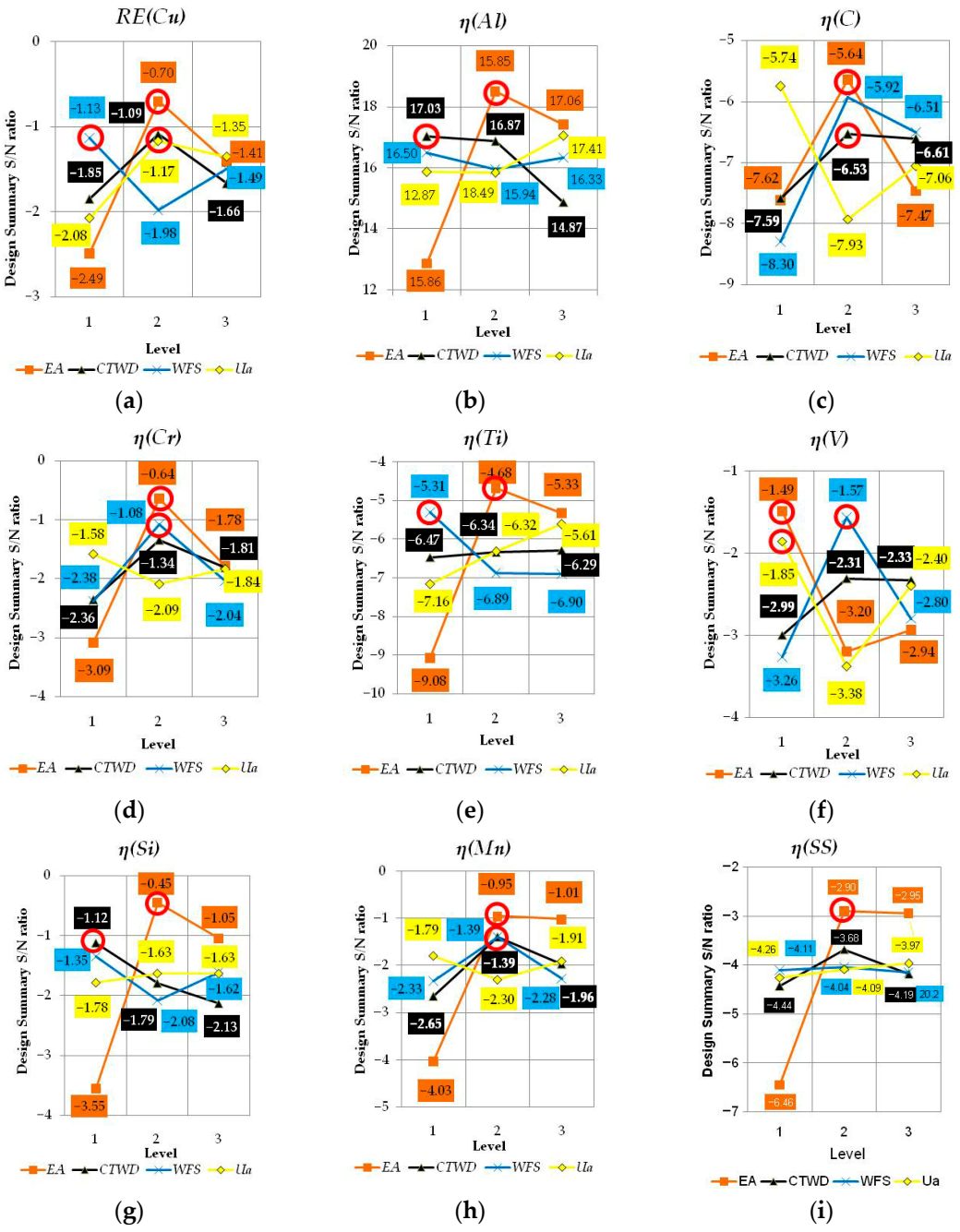

Figure 4. Main effects diagram for signal-to-noise ratio for element transfer coefficients: (**a**) copper recovery coefficient *RE*(*Cu*); (**b**) aluminium transfer coefficient $\eta(Al)$; (**c**) carbon transfer coefficient $\eta(C)$; (**d**) chrome transfer coefficient $\eta(Cr)$; (**e**) titanium transfer coefficient $\eta(Ti)$; (**f**) vanadium transfer coefficient $\eta(V)$; (**g**) silicon transfer coefficient $\eta(Si)$; (**h**) manganese transfer coefficient $\eta(Mn)$; (**i**) total element transition coefficient $\eta(SS)$. Red circles indicate optimal levels for the most significant variables.

It was found that the wire feed speed had a significant effect on the transfer coefficients of carbon, vanadium, and chromium (see Figure 5a1,a2). This parameter contributed 35.65%, 32.45%, and 19.91% respectively Optimal *WFS* values were observed at a medium level of 1.85 m·min^{-1} (Figure 4c,d,f). Additionally, a significant influence of wire feed speed on both the titanium transfer coefficient and the copper recovery factor was identified (see Figure 5a1,a2).

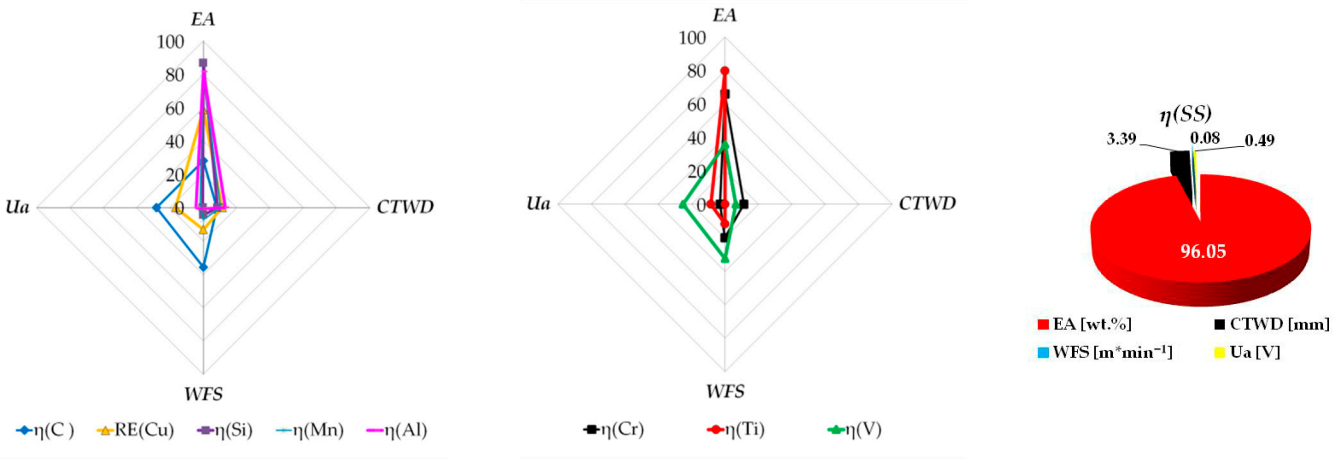

(**a1**) (**a2**) (**b**)

Figure 5. (**a1**,**a2**) Radar graph showing the interaction between factors of for element transition and pie charts showing the contribution of variables to the (**b**) total element transfer coefficient $\eta(SS)$.

The voltage set on the power source, a parameter of the hardfacing process, influenced the transfer coefficients of carbon and vanadium (see Figure 5), as well as the copper recovery factor (see Figure 5a1). The optimal U_{set} values were ensured at the average level of U_{set} = 31 V (see Figure 4a,c). This was indicated by the high signal-to-noise ratio values (Figure 4a). However, the highest transfer coefficients of vanadium were achieved at a lower voltage level of U_{set} = 28 V (see Figure 4f).

3.2.3. Factorial Design Analysis of Element Transfer Coefficient

Regression models of melting characteristics are represented by Equations (14)–(22):

$$Y_{(\eta(C))} = -0.03 - 0.00043 \times EA^2 + 8.87282 \times WFS - 1.546 \times WFS^2 - \\ -0.87282 \times U_{ser} + 2.00244 \times U_{set}^2 + 0.01155 \times EA \times WFS - 0.10454 \times WFS \times U_{ser}, \quad (14)$$

$$Y_{(\eta(Cr))}, = 1.5742 - 0.27364 \times EA + 0.0001 \times EA^2 - 0.6198 \times WFS^2 - \\ +0.202626 \times EA \times WFS + 0.002 \times EA^2 \times WFS - 0.00158 \times EA^2 \times WFS^2 \quad (15)$$

$$Y_{(\eta(Th))}, = -1.31362 + 0.12283 \times EA - 0.00137 \times EA^2 + 0.29629 \times WFS - \\ -0.01947 \times EA \times WFS \quad (16)$$

$$Y_{(\eta(V))} = 1.589137 - 0.054945 \times EA + 0.000874 \times EA^2 + 0.29629 \times WFS^2 - \\ -0.01947 \times U_{set}^2, \quad (17)$$

$$Y_{(\eta(Si))}, = 1.99114 - 0.08777 \times EA + 0.002114 \times EA^2 - 0.067643 \times CTWD + \\ +0.004779 \times EA \times CTWD + 0.000003 \times EA \times CTWD^2 - 0.000096 \times EA^2 \times CTWD \quad (18)$$

$$Y_{(\eta(Mn))}, = -10.3725 + 0.4838 \times EA - 0.009 \times EA^2 + 0.3737 \times CTWD - \\ -0.0032 \times CTWD^2 - 0.0099 \times EA \times CTWD + 0.0002 \times EA^2 \times CTWD \quad (19)$$

$$Y_{(\eta(Al))}, = 1.4729 - 0.039338 \times EA + 0.000622 \times EA^2 - \\ -0.041132 \times CTWD + 0.000561 \times CTWD^2 \quad (20)$$

$$Y_{(RE(Cu))} = -9.23274 + 0.07505 \times EA - 0.00121 \times EA^2 + 0.31305 \times WFS^2 + \\ +0.58559 \times U_{set} + 0.000561 \times U_{wet}^2 - 0.03921 \times EA \times WFS + 0.00228 \times EA \times U_{set}, \quad (21)$$

$$Y_{(\eta(SS))}. = -3.49774 + 0.07985 \times EA - 0.00121 \times EA^2 + \\ +0.58559 \times CTWD + 0.000561 \times CTWD^2 \quad (22)$$

Table 7 displays the coefficients of determination (R^2) and the adjusted sums of squares (R Adj) for each developed mathematical model. The quality of these models is rated as 'very good,' supported by the high values of the coefficients of determination and adjusted sums of squares.

Table 7. Result of analysis of variance for the applied conditions on element transfer coefficients and recovery fact.

Criteria	Mathematical Model				
	$Y_{\eta(c)}$	$Y_{\eta(cr)}$	$Y_{\eta(Ti)}$	$Y_{\eta(V)}$	
Coefficient of Determination (R sqr)	0.99999	0.98226	0.90705	0.86763	
Adjusted Sum of Squares (R Adj)	0.99995	0.92904	0.8141	0.73526	
Model quality	Very good	Very good	Good	Good	
Criteria	**Mathematical Model**				
	$Y_{\eta(Si)}$	$Y_{\eta(Mn)}$	$Y_{\eta(Al)}$	$Y_{RE(Cu)}$	$Y_{\eta(SS)}$
Coefficient of Determination (R sqr)	0.9971	0.9951	0.97003	0.99912	0.99406
Adjusted Sum of Squares (R Adj)	0.9884	0.98039	0.94005	0.99299	0.98811
Model quality	Very good	Very good	Very good	Very good	Very good

The obtained data demonstrated that the developed mathematical models exhibited very good or good performance. This is also confirmed by the plots of observed versus predicted values constructed for the models (see Figure 6). The models' predictive accuracy is indicated by the close proximity of the predicted data points to the diagonal red line. All models showed excellent quality, except for those describing the vanadium and titanium transfer coefficients (Figure 6e,f).

A Pareto chart (see Figure 7) was used to present the results, which were evaluated using analysis of variance (ANOVA).

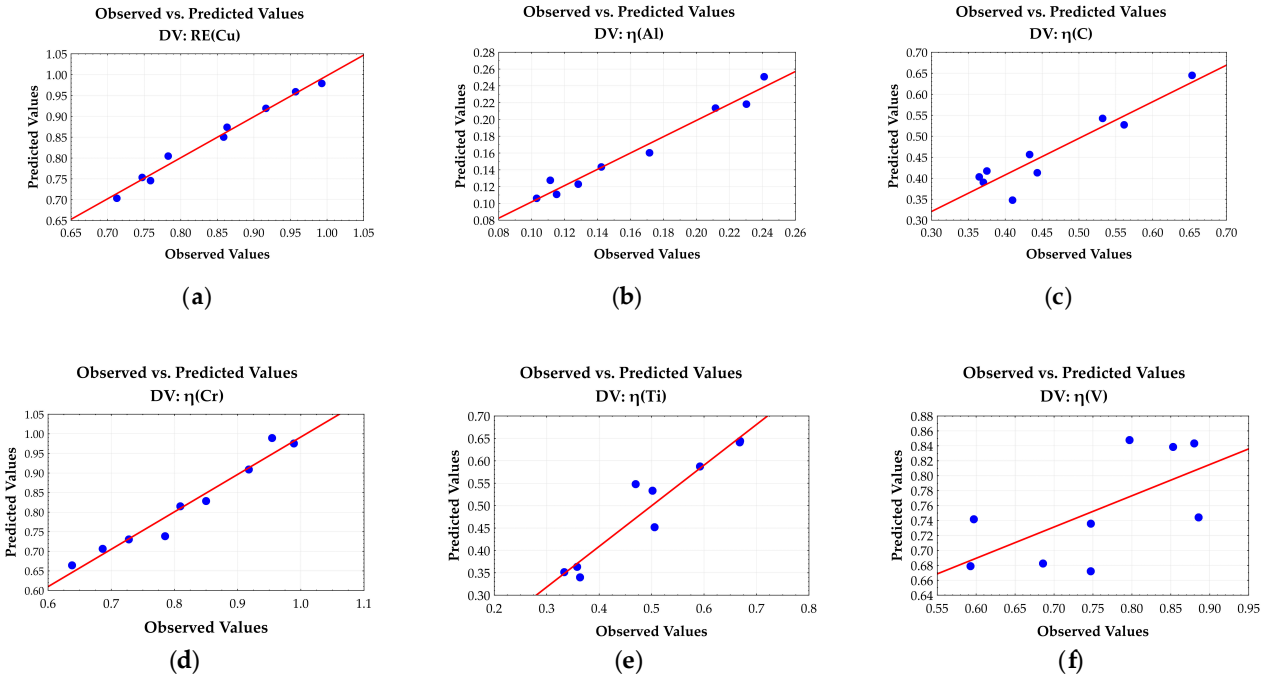

Figure 6. *Cont.*

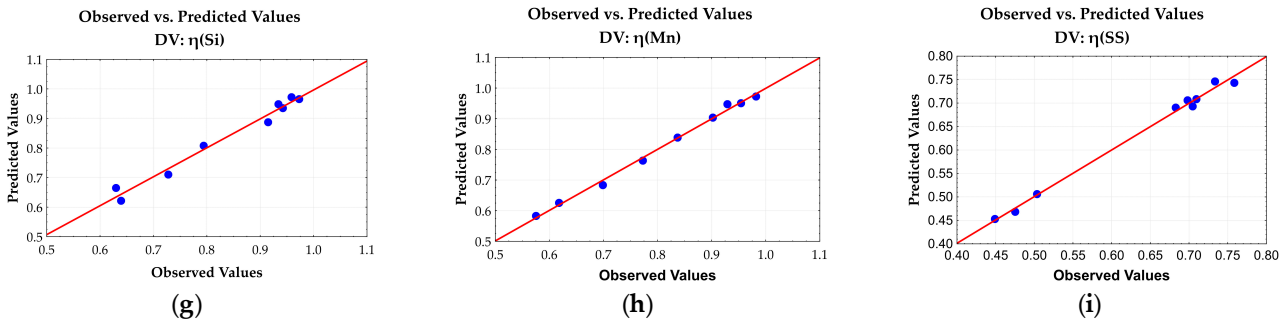

Figure 6. Predicted and observed values of the dependent variable for element transfer coefficients: (**a**) copper recovery factor *RE*(*Cu*); (**b**) aluminium transfer coefficient $\eta(Al)$; (**c**) carbon transfer coefficient $\eta(C)$; (**d**) chrome transfer coefficient $\eta(Cr)$; (**e**) titanium transfer coefficient $\eta(Ti)$; (**f**) vanadium transfer coefficient $\eta(V)$; (**g**) silicon transfer coefficient $\eta(Si)$; (**h**) manganese transfer coefficient $\eta(Mn)$; (**i**) total element transition Coefficient $\eta(SS)$.

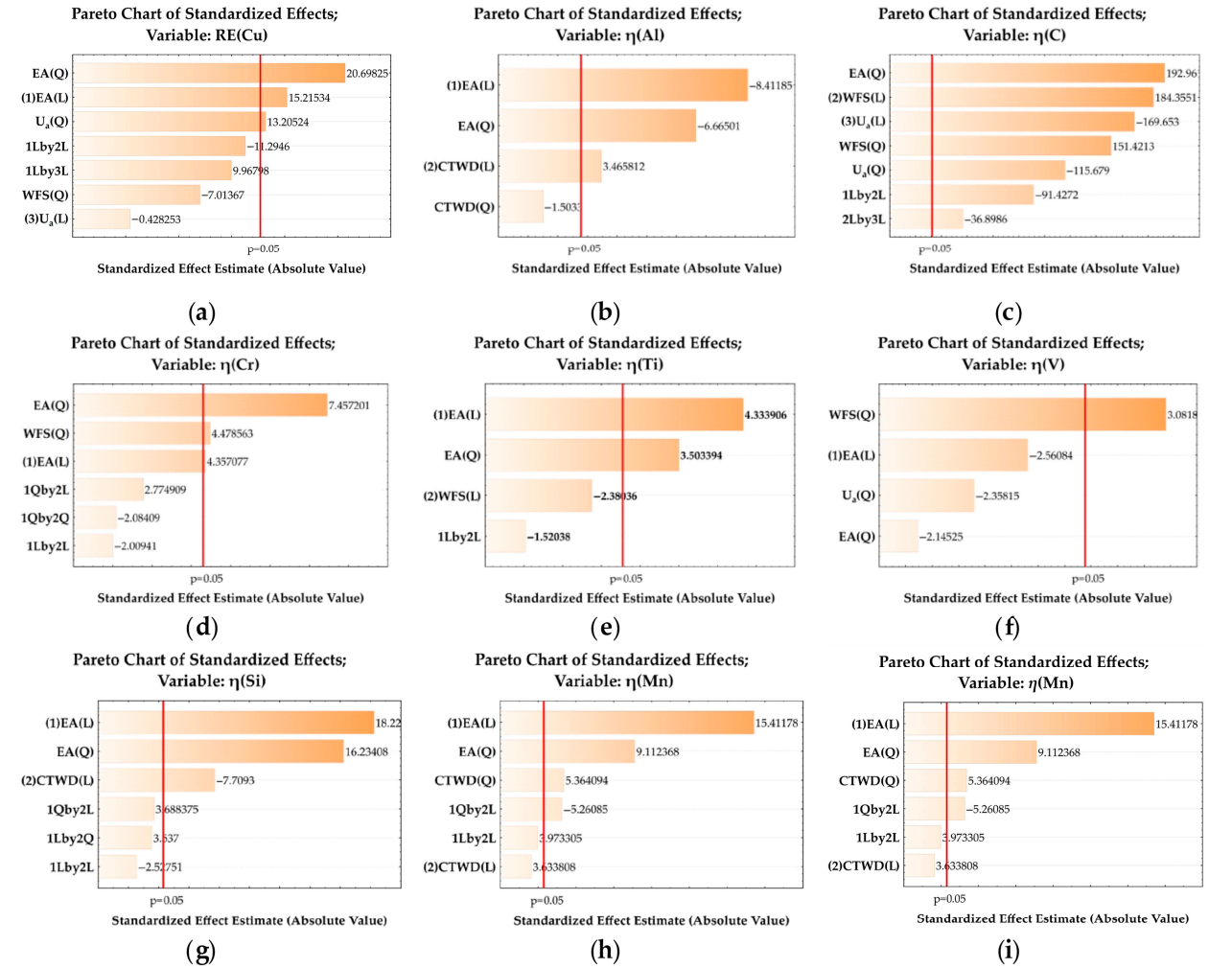

Figure 7. Pareto chart of the influence of the terms of the equations for the most significant variables, for weld bead morphology parameters: (**a**) copper recovery factor *RE*(*Cu*); (**b**) aluminium transfer coefficient $\eta(Al)$; (**c**) carbon transfer coefficient $\eta(C)$; (**d**) chrome transfer coefficient $\eta(Cr)$; (**e**) titanium transfer coefficient $\eta(Ti)$; (**f**) vanadium transfer coefficient $\eta(V)$; (**g**) silicon transfer coefficient $\eta(Si)$; (**h**) manganese transfer coefficient $\eta(Mn)$; (**i**) total element transfer coefficient $\eta(SS)$.

Figure 7 presents Pareto charts illustrating the relative influence of the regression equation terms on copper recovery and elemental transfer coefficients in the weld bead.

For all considered responses, the main effects dominated over interaction and quadratic terms, indicating that the elemental transfer was primarily governed by individual process parameters rather than their combined effects. The results obtained showed that the terms of the regression equation linked to the percentage of exothermic addition in the core filler had the greatest effect on the elemental transfer coefficients.

Figures 8 and 9 show the response surfaces of the mathematical model illustrating the relationship between the transition element and the parameters of the hardfacing modes, as well as the content of the exothermic addition in the core filler.

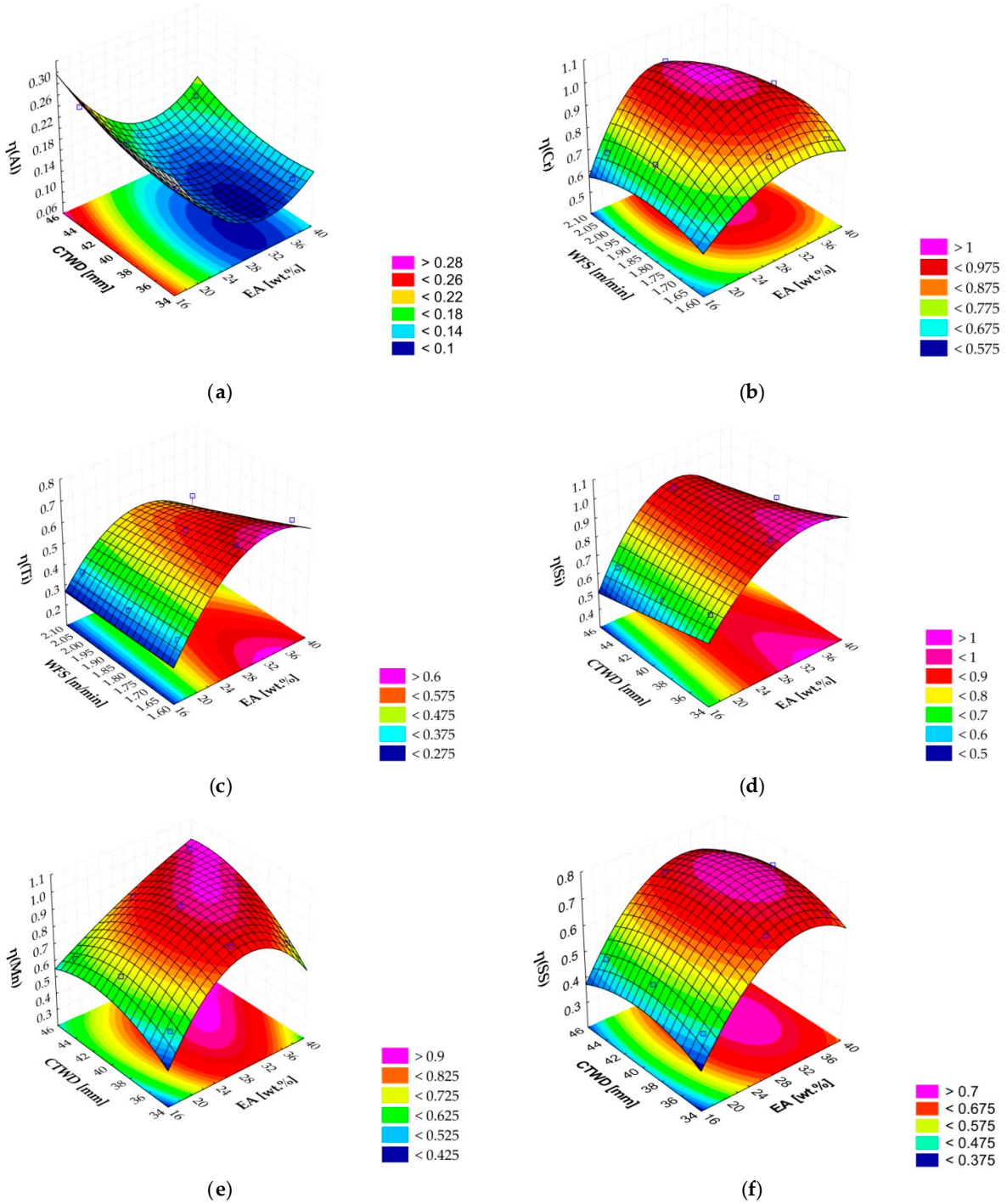

Figure 8. Response surfaces plot for (**a**) aluminium transfer coefficient $\eta(Al)$; (**b**) chrome transfer coefficient $\eta(Cr)$; (**c**) titanium transfer coefficient $\eta(Ti)$; (**d**) silicon transfer coefficient $\eta(Si)$; (**e**) manganese transfer coefficient $\eta(Mn)$; (**f**) total element transition coefficient $\eta(SS)$.

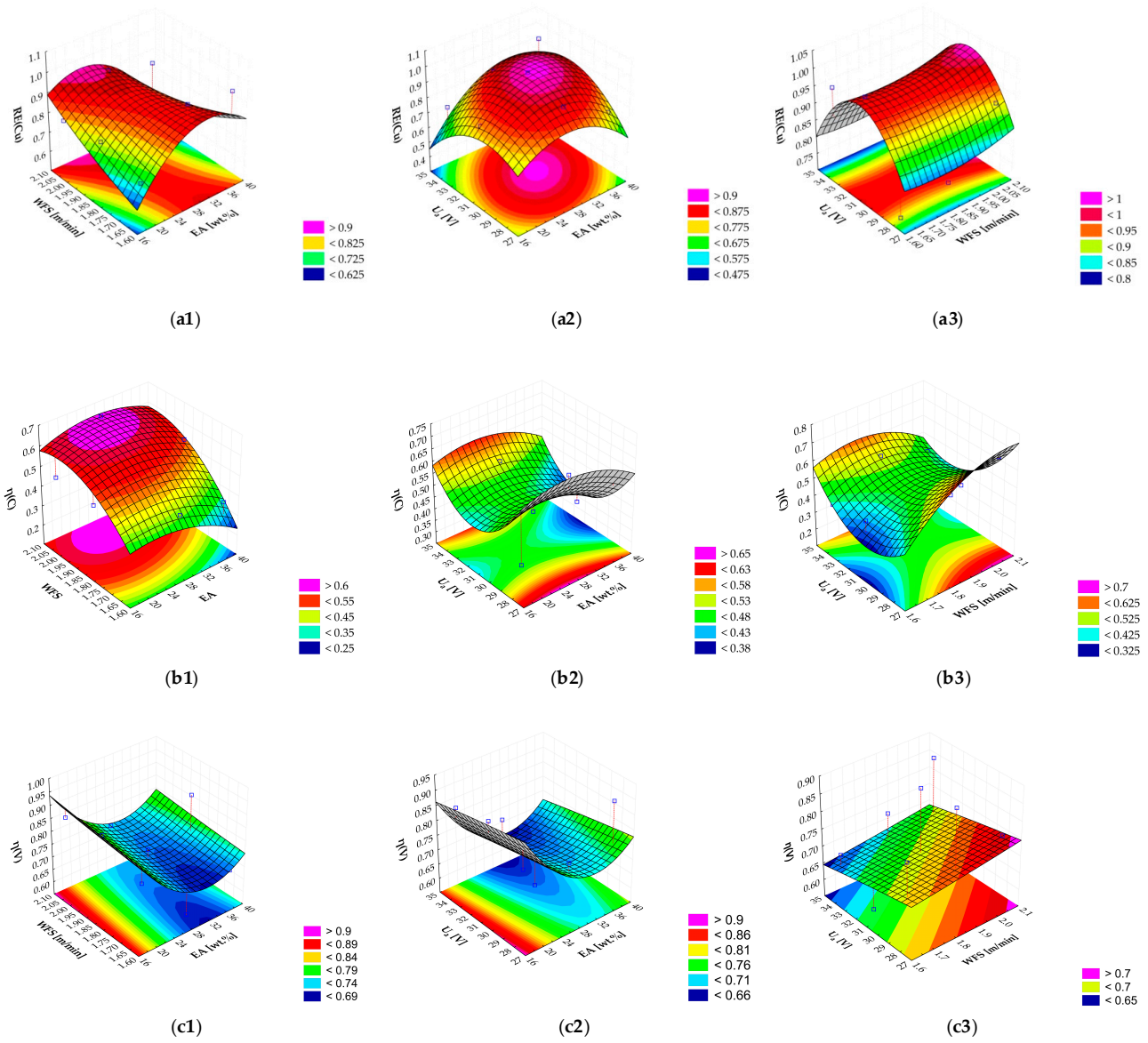

Figure 9. Response surface with three slump levels for: copper recovery coefficient *RE*(*Cu*) (**a1**) high of percentage of exothermic mixture in the core filler (*EA* = 38 wt.%), (**a2**) high of contact tip-to-work distance (*CTWD* = 45 mm) and (**a3**) medium of set voltage on the power source (U_{set} =31 V); carbon transfer coefficient $\eta(C)$ (**b1**) high of percentage of exothermic mixture in the core filler (*EA* = 38 wt.%), (**b2**) high of contact tip-to-work distance (*CTWD* = 45 mm) and (**b3**) medium of set voltage on the power source (U_{set} =31 V); vanadium transfer coefficient $\eta(V)$ (**c1**) high of percentage of exothermic mixture in the core filler (*EA* = 38 wt.%), (**c2**) high of contact tip-to-work distance (*CTWD* = 45 mm) and (**c3**) medium of set voltage on the power source (U_{set} = 31 V).

3.3. Welding Thermal Cycle Parameters

During FCAW-S hardfacing, the thermal cycle of the weld was primarily governed by heat input, peak temperature, and cooling rate. These factors determined the evolution of the deposited metal and the degree to which it was diluted with the base material. These factors ultimately determined the microstructure of the deposited metal and its mechanical and service properties. Increased heat input and slower cooling rates usually resulted in grain coarsening and increased dilution. On the other hand, a reduction in heat input could lead to the formation of a finer microstructure and an increase in hardness [125]. The thermal cycle was described by three key parameters: heat input (*HI*), cooling rate (*CR*),

and cooling time $\Delta t_{8/5}$. Heat input (*HI*) is the quantity of energy introduced from the arc per unit length of weld. The heat input was calculated by means of Equation (23) [114]:

$$HI = \frac{60 \times \eta_{FCAW} \times U_{set} \times I}{1000 \times TS} \quad (23)$$

where *HI* is heat input, (kJ/mm); η_{FCAW} is the coefficient of efficiency of the process $\eta_{\mathrm{FCAW}} = 0.75$.

The cooling rate (*CR*) and cooling time ($\Delta t_{8/5}$) were calculated using Equations (24) and (25) [112,114].

$$CR_{8.5} = \frac{\Delta T_{8/5}}{\Delta t_{8/5}}, \quad (24)$$

$$\Delta t_{8.5} = \frac{E \cdot}{2 \cdot \pi \cdot k} \cdot \left[\frac{1}{500 - T_0} - \frac{1}{800 - T_0} \right], \quad (25)$$

where $\Delta T_{8/5}$ was the temperature variation within the selected range of 800 and 500 °C, *E* is welding energy (kJ·cm^{-1}), λ is material thermal conductivity λ = 42 J/(s·m·C) [114], and T_0 is the initial temperature of the plate T_0 = 25 °C.

3.3.1. Experiment Results for Welding Thermal Cycle Parameters

Table 8 shows the experimental results for the thermal cycle parameters and hardness of all alloys across nine experiments.

Table 8. Experimental and calculated values of welding thermal cycle parameters.

№ Exp.	Heat Input				Cooling Time			
	***HI*(*e*)**	***HI*(*c*)**	**Diff.**	**Dev. %**	**$\Delta t_{8/5}$(*e*)**	**$\Delta t_{8/5}$(*c*)**	**Diff.**	**Dev. %**
1	1.237665	1.269883	−0.032218	2.60	5.755207	5.963896	−0.208689	3.63
2	1.259300	1.332659	−0.073359	5.83	5.855807	6.063564	−0.207757	3.55
3	1.778054	1.746563	0.031492	1.77	8.268044	8.196100	0.071944	0.87
4	1.418210	1.381530	0.036680	2.59	6.594749	6.490871	0.103878	1.58
5	1.547082	1.515590	0.031492	2.04	7.194009	7.122065	0.071944	1.00
6	1.601868	1.537432	0.064436	4.02	7.448766	7.031389	0.417378	5.60
7	1.568093	1.631077	−0.062983	4.02	7.291714	7.435601	−0.143887	1.97
8	1.772763	1.804981	−0.032218	1.82	8.243437	8.452125	−0.208689	2.53
9	1.320467	Hardness	0.036680	2.78	6.140238	6.036360	0.103878	1.69

№ Exp.	Cooling rate				Hardness						
	***CR*(*e*)**	***CR*(*c*)**	**Diff.**	**Dev. %**	**1**	**2**	**3**	***HV*(*e*)**	***HV*(*c*)**	**Diff.**	**Dev.%**
1	52.12671	50.79853	1.32817	2.55	571	538	514	541.0	539.3	1.7	0.32
2	51.23119	48.52666	2.70454	5.28	648	677	514	613.0	594.3	18.7	3.06
3	36.28428	37.00087	−0.71659	1.97	546	546	514	535.3	547.4	−12.1	2.25
4	45.49074	46.84301	−1.35227	2.97	489	563	493	515.0	500.6	14.4	2.79
5	41.70137	42.41796	−0.71659	1.72	464	352	292	369.3	378.3	−9.0	2.44
6	40.27513	42.93147	−2.65635	6.60	390	497	724	537.0	556.6	−19.6	3.65
7	41.14259	39.70941	1.43318	3.48	565	550	593	569.3	568.5	0.9	0.15
8	36.39259	35.06441	1.32817	3.65	677	824	756	752.3	754.6	−2.3	0.31
9	48.85804	50.21031	−1.35227	2.77	401	401	420	407.3	400.0	7.3	1.79

3.3.2. Taguchi Method and ANOVA for Welding Thermal Cycle Parameters

Figure 10 shows the main effects of the signal-to-noise (S/N) ratio for each of the parameters investigated. The 'smaller-is-better' criterion was applied to heat input and cooling time, while the 'higher-is-better' criterion was applied to cooling rate and hardness.

The resulting plots demonstrate the robustness of the experimental design and the reliability of the obtained results. Red circles indicate the levels that achieve the best S/N ratios.

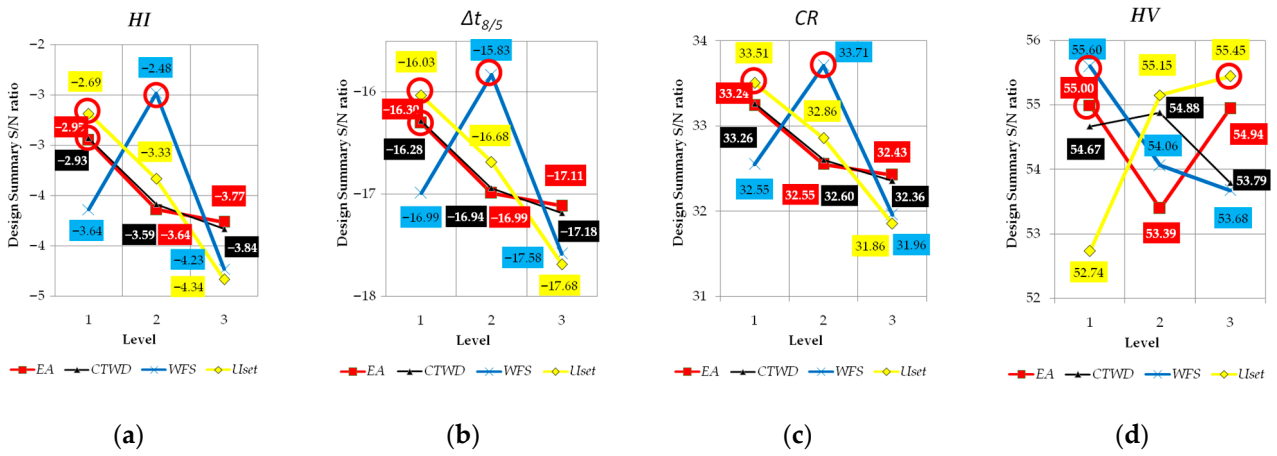

Figure 10. Main effects diagram for signal-to-noise ratio for melting characteristics: (**a**) heat input *HI*; (**b**) cooling time $\Delta t_{8/5}$; (**c**) cooling rate *CR*; (**d**) hardness *HV*. Red circles indicate optimal levels for the most significant variables.

The optimal parameters and the results of the analysis of variance (ANOVA) are shown in Figure 11.

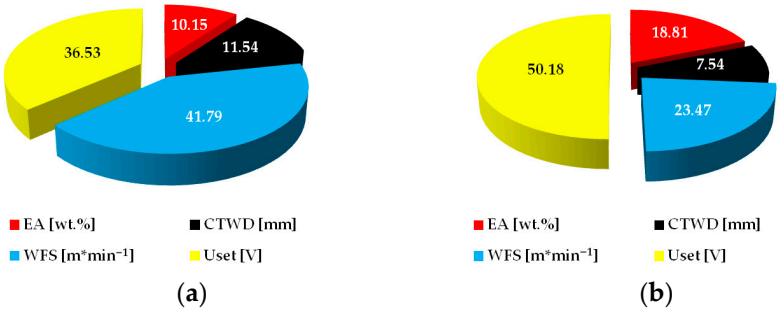

Figure 11. Pie charts showing the contribution of variables to each element transfer coefficients: (**a**) heat input *HI*, cooling time $\Delta t_{8/5}$, and cooling rate *CR*; (**b**) hardness *HV*.

Analysis of the data presented in Figure 11a revealed that the two main factors influencing the parameters that define the welding thermal cycle were wire feed speed and voltage set on the power source. These two parameters accounted for 41.79% and 36.53% of the total variation, respectively. The influence of the other two parameters—namely, *EA* and *CTWD*—was minor and could be considered indirect, acting through their effect on the two dominant parameters. The optimal conditions differed for the three parameters of the welding thermal cycle (Figure 10a–c) and were achieved at a medium wire feed speed (WFS = 1.85 m·min^{-1}), a low voltage set on the power source (U_{set} = 28 V), as well as low values of exothermic addition in the core filler (EA = 20 wt.%) and a low contact tip to work distance ($CTWD$ = 35 mm) (see Figure 10).

As shown in Figure 11b, the voltage set on the power source had the greatest influence on the hardness of the deposited metal, while the wire feed speed and the percentage of exothermic addition in the core filler had a smaller effect. These factors contributed 50.18%, 23.47%, and 18.81% respectively. The optimal voltage setting for hardness differed from that for the welding thermal cycle parameters and was observed at U_{set} = 34 V; EA = 20 wt.%; and WFS = 1.63 m·min^{-1}.

3.3.3. Factorial Design Analysis of Welding Thermal Cycle Parameters

Following the ANOVA-based elimination of insignificant variables, the regression models were established as follows:

$$Y_{HI} = -95.4008 + 100.1886 \times WFS - 26.0396 \times WFS^2 + \\ +3.6992 \times U_{ser} - 3.8646 \times WFS \times U_{ser} + 1. - 129 \times WFS^2 \times U_{ser}, \quad (26)$$

$$Y_t = -443.619 + 0.27364 \times WFS - 121.085 \times WFS^2 + 17.202 \times U_{ser} - \\ -18.715 \times WFS \times U_{ser} + 0.012 \times WFS \times U_{set}^2 - 0.00158 \times WFS^2 \times U_{ser}, \quad (27)$$

$$Y_{CR} = 2497.08 - 2497.84 \times WFS + 639.83 \times WFS^2 - 95.49 \times U_{ser} + \\ +98.66 \times WFS \times U_{ser} - 25.59 \times WFS^2 \times U_{ser}, \quad (28)$$

$$Y_{(\eta(V))} = -7115.16 - 1.6 \times EA^2 - 237.42 \times WFS + 597.27 \times U_{ser} - \\ -12.72 \times U_{set}^2 - 9.54 \times EA \times WFS^2 + 0.07 \times EA^2 \times U_{ser} + 1.26 \times WFS \times U_{set}^2. \quad (29)$$

The parameters characterising the quality of the developed models are summarised in Table 9.

Table 9. Result of analysis of variance for the applied conditions on welding thermal cycle parameters.

Criteria	Mathematical Model			
	Y_{HI}	Y_t	Y_{CR}	Y_{TV}
Coefficient of Determination (R sqr)	0.93948	0.97587	0.91451	0.99743;
Adjusted Sum of Squares (R Adj)	0.83862	0.90349	0.77203	0.97945
Model quality	Good	Very good	Good	Good

The regression models developed for all the investigated welding thermal cycle parameters were statistically significant and adequate, as confirmed by the ANOVA results (Table 9). The coefficients of determination (R^2) are greater than 0.91 for all responses, showing a strong agreement with the experimental data. The mathematical models developed for heat input (*HI*) and cooling rate (*CR*) demonstrate stable approximation quality, with the highest model accuracy achieved for hardness (*HV*).

The predictive capability of the developed regression model was further verified by analysing the level of consistency between experimentally obtained data and model-estimated responses. The graphs in Figure 12 show the change in observed efficiency as a function of predicted efficiency for each of the mathematical models that were developed.

Figure 12a–d shows a close agreement between the experimental and predicted values for all dependent variables, indicating a high level of agreement with the line of equality. A uniform distribution of data points along the regression line is observed for *HI* and cooling time $\Delta t_{8/5}$, indicating the absence of systematic model errors.

Figure 13 illustrates the outcome of the Pareto analysis, with the contribution of each parameter to the overall response expressed through the length of the standardised effect bars.

The plots that were obtained provide confirmation of the results of the ANOVA analysis for the welding thermal cycle parameters and hardness. The most significant effects were associated with the regression terms relating to wire feed speed and the voltage set on the power source. The Pareto chart (Figure 13d) shows that the linear effects of the welding process parameters, especially wire feed speed and arc voltage, had a significantly more pronounced influence on the hardness of the deposited metal. These effects were statistically significant. This indicated that the structural and mechanical properties of the welded joint were highly sensitive to variations in the thermal cycle.

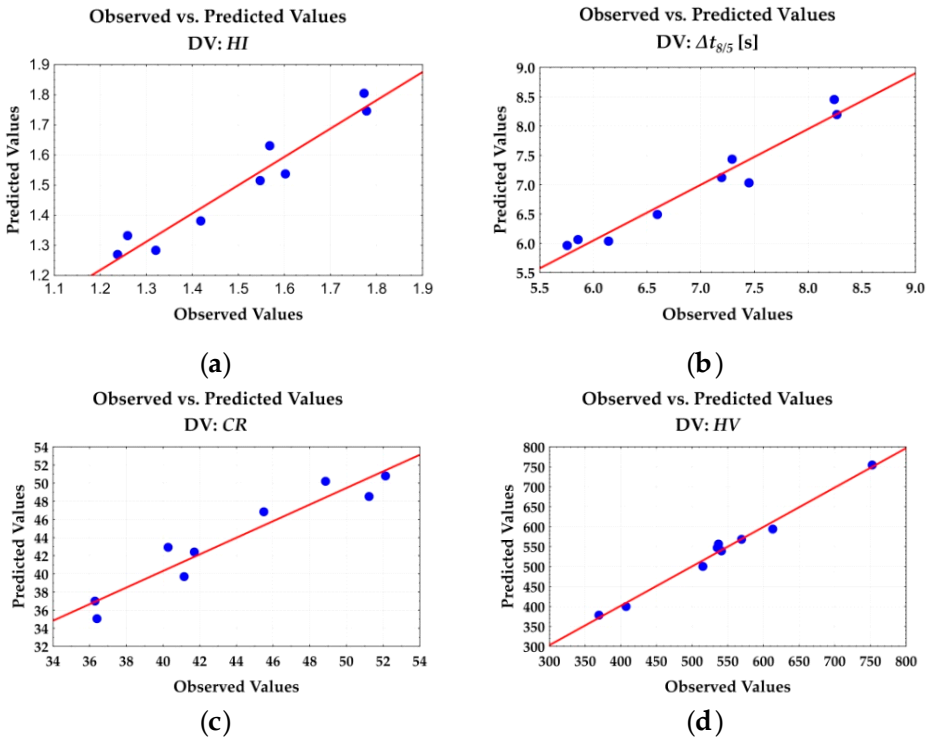

Figure 12. Predicted and observed values of the dependent variable for welding thermal cycle parameters: (**a**) heat input *HI*; (**b**) cooling time $\Delta t_{8/5}$; (**c**) cooling rate *CR*; (**d**) hardness *HV*.

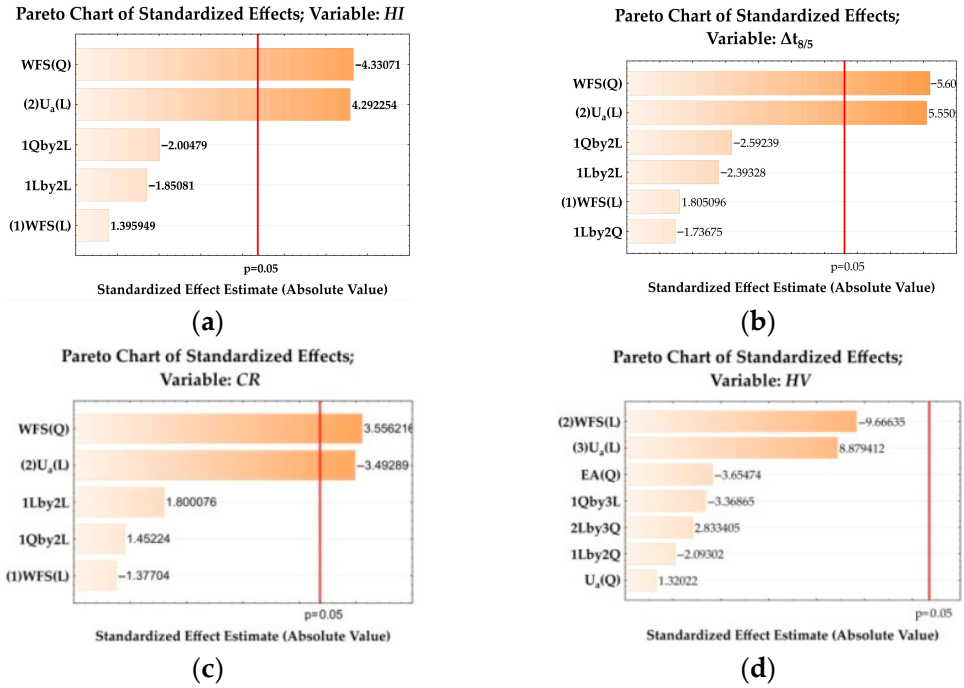

Figure 13. Pareto chart of the influence of the terms of the equations for the most significant variables, for welding thermal cycle parameters: (**a**) heat input *HI*; (**b**) cooling time $\Delta t_{8/5}$; (**c**) cooling rate *CR*; (**d**) hardness *HV*.

Figures 14 and 15 show the response surfaces of the mathematical model of the dependence of the hardfacing thermal cycle parameters on the parameters of the hardfacing modes.

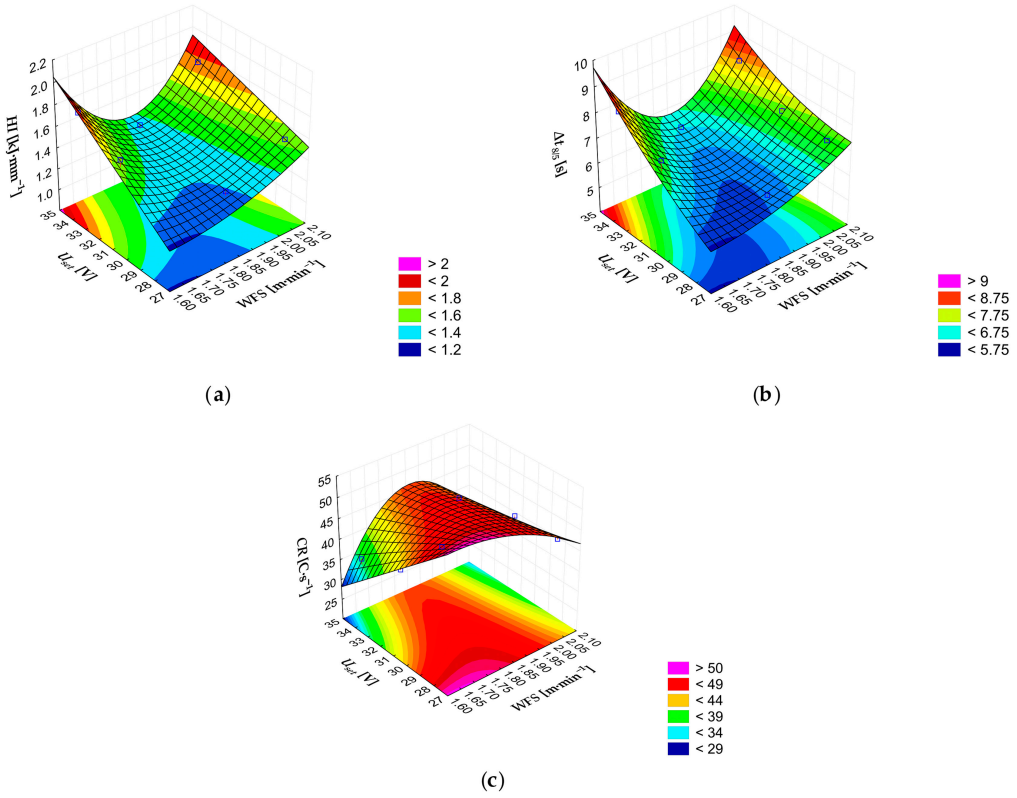

Figure 14. Pareto Response surfaces plotfor welding thermal cycle parameterseat input *HI*; (**b**) cooling time $\Delta t_{8/5}$; (**c**) cooling rate *CR*.

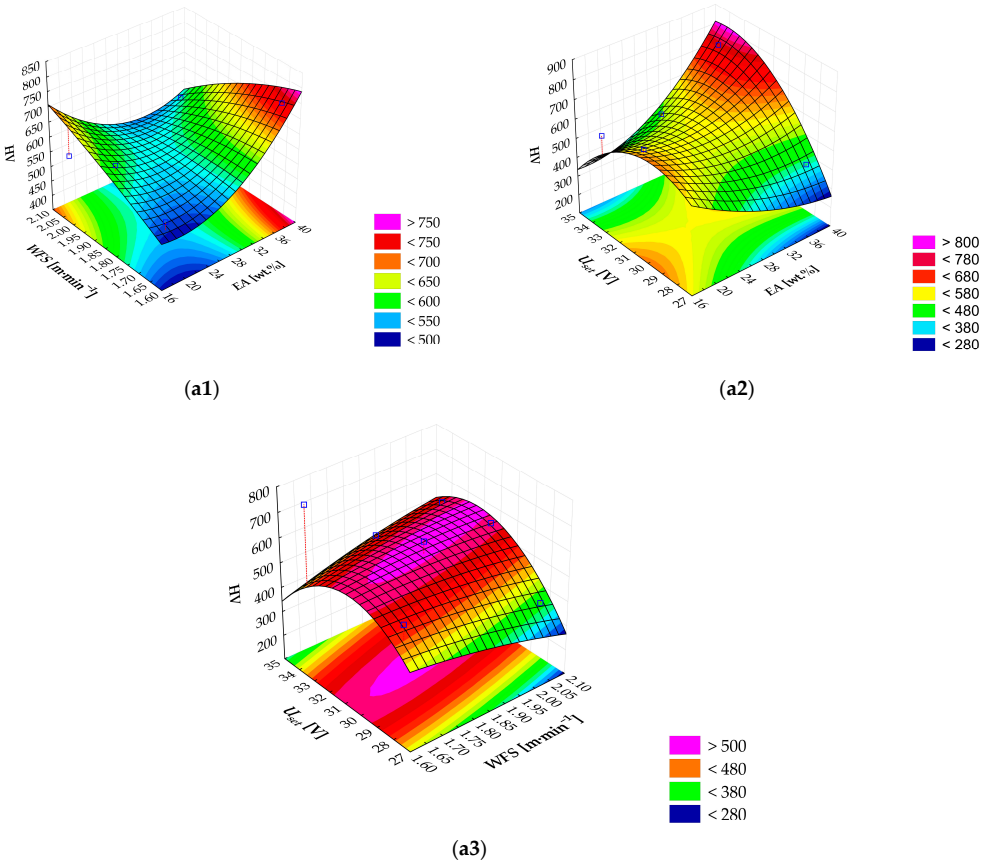

Figure 15. Response surface of hardness with three slump levels for (**a1**) high percentage of exothermic mixture in the core filler (*EA* = 38 wt.%), (**a2**) medium set voltage on the power source (U_{set} =31 V), and (**a3**) medium wire feed speed (*WFS* = 2.07 m·min^{-1}).

3.4. Taguchi–Grey Relational Analysis Coupled with Principal Component Analysis

The normalised values and deviation sequence are shown in Table 10.

Table 10. Normalised data of response characteristics.

№ Exp.	DR_n	SF_n	$RE(Cu)_n$	HV_n
1	0.000000	0.179293	0.000000	0.448303
2	0.312500	0.356061	0.250000	0.636292
3	0.500000	0.164141	0.164286	0.433420
4	0.710938	0.109848	0.535714	0.380418
5	0.929688	0.000000	0.725000	0.000000
6	0.492187	0.643939	1.000000	0.437859
7	1.000000	0.747475	0.521429	0.522193
8	0.078125	0.393939	0.871429	1.000000
9	0.742188	1.000000	0.121429	0.099217

The values of the principal-component loadings for each response were presented in Table 11.

Table 11. PCA Components (Loadings).

Principal Component	*MOR*	*DR*	*RE(Cu)*	*HV*
PC1	0.794408	0.297909	0.085891	−0.522292
PC2	0.079026	0.094945	0.936443	0.328352
PC3	−0.152286	0.933592	−0.177093	0.271759
PC4	0.582649	−0.175047	−0.290405	0.738609

The computation of grey relation grades (GRGs) after introducing PCA and the weighted value of each performance characteristic. Table 12 showed the GRGs and rank.

Table 12. Grey relational grades.

№ Exp.	*GRA*	*Rank*
1	0.381411	9
2	0.461184	7
3	0.431601	8
4	0.491173	6
5	0.548312	5
6	0.630416	3
7	0.675005	1
8	0.650770	2
9	0.592357	4

The GRA results indicate that the optimal experimental runs are Exp. 7 (Rank 1), Exp. 8 (Rank 2), and Exp. 6 (Rank 3). Their GRGs are relatively close, with values of 0.675005, 0.650770, and 0.630416, respectively. Analysis of the experimental data for these runs revealed that Exp. 8 has a lower deposition rate (DR = 3.98 kg·h^{-1}) than Exp. 7 (DR = 5.16 kg·h^{-1}) and Exp. 6 (DR = 4.51 kg·h^{-1}). However, it demonstrates the highest hardness. Furthermore, the analysis showed that the P3-E1-7 weld metal specimen (Exp. 7) had a higher hardness than the P3-E1-6 specimen (569 HV vs. 537 HV). These findings confirm the effectiveness of the GRA approach for multi-objective optimisation. The optimal parameters identified are as follows: EA = 38 wt.%, $CTWD$ = 35 mm, WFS = 2.07 m·min^{-1}, and U_{set} = 31 V.

3.5. The Microstructure of Welded Metal Samples Is Analysed

3.5.1. Theoretical Analysis and Phase Stability Simulation of Microstructure by JMatPro

A phase diagram simulating the phase ratio at a given temperature was created based on the chemical composition, using the simulation software JMatPro® API v7.0 (Figure 16). The resulting phase diagram provides approximate information about the critical temperatures at which individual phase transformations occur.

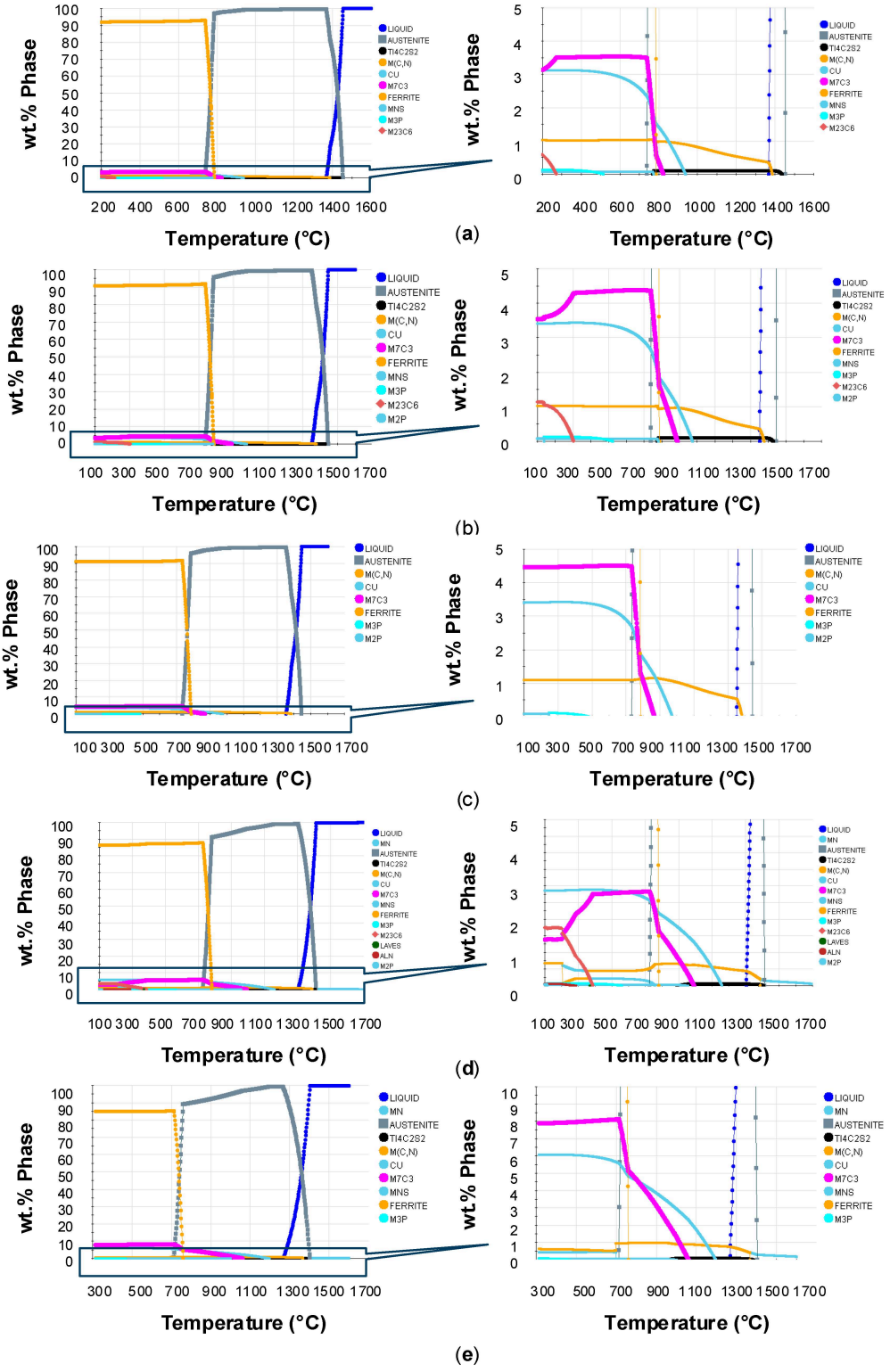

Figure 16. *Cont.*

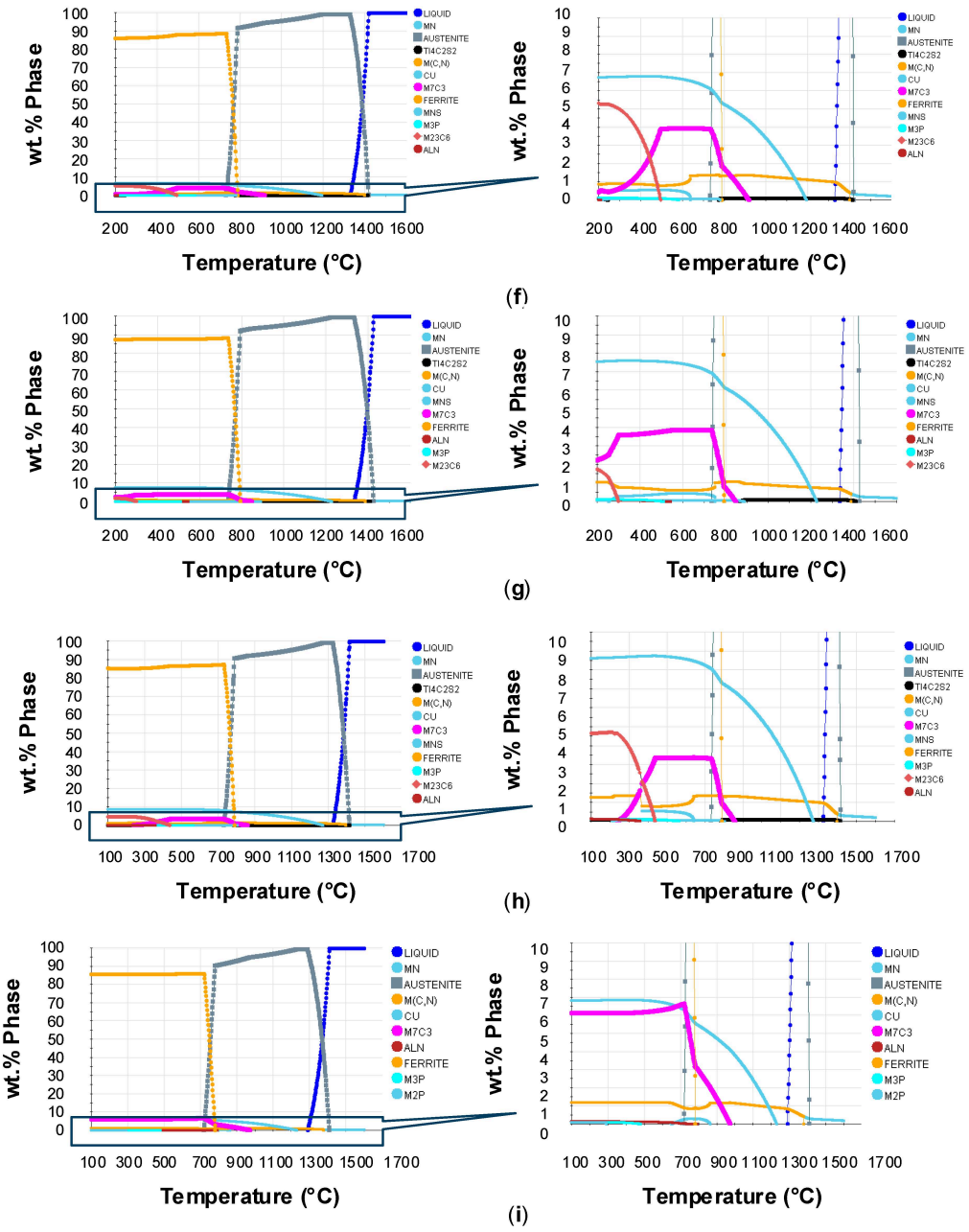

Figure 16. Calculation and prediction of phase type and changes of elements in the plain carbon steel region using JMatPro software. Equilibrium phase diagram for deposited metal samples: (**a**) P3-E1-1, (**b**) P3-E1-2, (**c**) P3-E1-3; (**d**) P3-E1-4, (**e**) P3-E1-5, (**f**) P3-E1-6; (**g**) P3-E1-7, (**h**) P3-E1-8, and (**i**) P3-E1-9.

The equilibrium phase diagrams calculated for the deposited metal samples are shown in Figure 16a–i.

For a better understanding of phase structural changes in alloys, phase changes and chemical element distribution were additionally analysed for one of the alloys (see Figure 17).

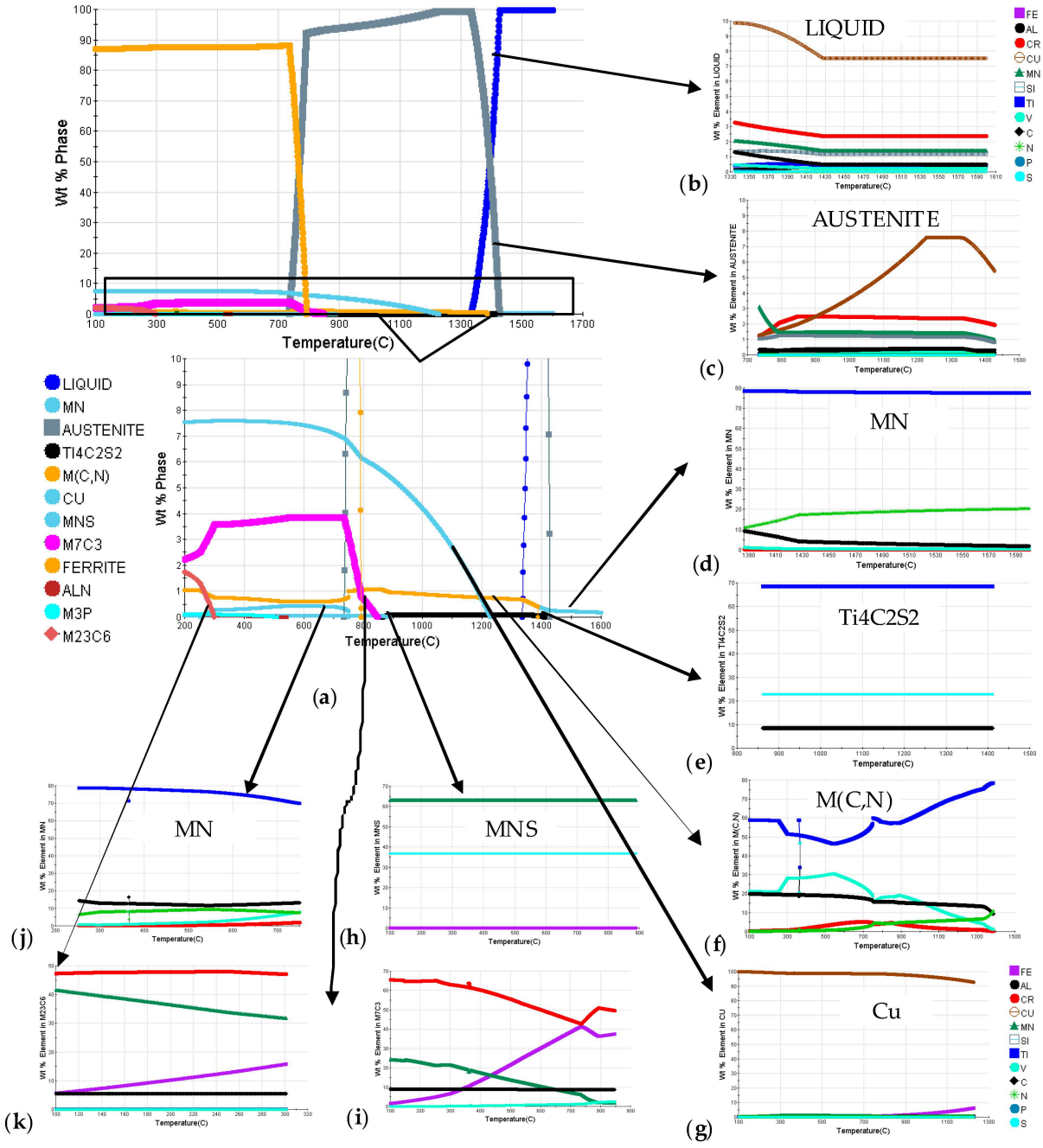

Figure 17. Calculation and prediction of phase type (**a**) and change in phase composition: (**b**) liquid; (**c**) high-temperature Austenite; (**d**) MN; (**e**) Ti4C2S2; (**f**) M(C,N); (**g**) Cu; (**h**) MNS; (**i**) M7C3; (**j**) ow-temperature MN; (**k**) M23C6.

A wide solidification temperature range was observed for alloys with high carbon and copper content (P3-E1-5 and P3-E1-9). The lowest liquidus and solidus temperatures were exhibited by these alloys at the same time. For alloy P3-E1-5, the liquidus and solidus temperatures were $T_l(5)$ = 1403.47 °C and $T_s(5)$ = 1267.19 °C, respectively; for P3-E1-9, they were $T_l(9)$ = 1410.8 °C and $T_s(9)$ = 1290.09 °C. The presence of elevated copper content (in alloys P3-E1-6, P3-E1-7, and P3-E1-8) has two effects. Firstly, it reduces the solidus temperature. Secondly, it promotes the formation of Cu-rich phases. On the other hand, higher concentrations of carbide-forming elements have a slightly higher liquidus temperature-increasing effect (see Table 13).

Table 13. JMatPro predictions on the melting range of each phase (°C).

Alloy	T_l	T_s	ΔT
P3-E1-1	1454.73	1367.42	87.31
P3-E1-2	1446.56	1351.39	95.17
P3-E1-3	1445.72	1352.49	93.23
P3-E1-4	1445.72	1352.49	93.23
P3-E1-5	1403.47	1267.19	136.28
P3-E1-6	1420.22	1330.26	89.96
P3-E1-7	1427.6	1334.5	93.1
P3-E1-8	1416.33	1325.5	90.83
P3-E1-9	1410.80	1290.09	120.71

Where T_l: liquidus, T_s: solidus.

The MN solid phase is a high-temperature phase that is similar to titanium carbonitride (Ti(N,C)). It slowly becomes richer in vanadium and carbon, approaching the composition TiN·(V,Cr)C. This phase is retained in the deposited metal after complete cooling because of the welding conditions (Figure 17d). Since this phase was high temperature, it had a shape similar to a regular rhombohedral shape. The final portions of the liquid metal enriched in alloying elements (see Figure 17b) are known to form sulfides during the cooling process, which precipitate in the form of the Ti4C2S2 phase (see Figure 17a). This is consistent with the Ti2CS phase (see Figure 17e). This observation is consistent with reported results for titanium-containing steels [126], since this phase is more stable than MnS. During solidification, a small amount of MnS is produced as a result of partial decomposition. However, MC-type carbides (Ti- and V-rich) are the first to precipitate, with their fraction remaining below 1 wt.%. Once solidified, the austenitic phase will be heavily enriched with elements such as Cu, Cr, Mn, etc. (see Figure 17c for details). At temperatures of around 1200 °C, a copper phase (Figure 17a) consisting predominantly of copper precipitates within the matrix. This phase forms as copper precipitates with a body-centred cubic (BCC) structure that is embedded in a BCC iron matrix [127]. An increase in hardness and static strength is attributed to the presence of finely dispersed Cu precipitates, resulting from dispersion strengthening [128]. However, owing to the non-equilibrium state of the deposited metal caused by the high cooling rate, the copper dissolved in the austenitic phase does not fully precipitate [112,129].

Following solidification, a stable austenitic matrix (γ-phase) is formed within the temperature range of 1050–850 °C. The addition of Cu and Mn makes the austenite stability region bigger at lower temperatures (see Figure 16f–h). On the other hand, high C and Cr contents (inalloys P3-E1-4 and P3-E1-5) restrict this region due to the high-temperature stability of the carbides. In the temperature range of 950–850 °C, M_7C_3 carbides gradually precipitate from the austenitic solid solution. In Cr-rich compositions, the process is followed at lower temperatures by the precipitation of $M_{23}C_6$ carbides at grain boundaries.

Table 14 shows the numerical values for the onset of austenite phase transformations into pearlite, bainite, and ferrite, as well as the onset of martensite formation and transformation into 90% martensite for each sample.

Figure 18a–i shows that the onset curves of the pearlitic transformation (Ps) shift towards longer times and lower temperatures when the total content of alloying elements such as Cr, Mn, and Cu increases. This behaviour indicates a reduction in diffusion-controlled processes and an increase in the hardenability of steels. The pearlitic transformation in steels with a carbon content of around 0.50–0.58 wt.% and moderate alloying occurs at higher temperatures and shorter cooling times. However, for steels with a high carbon content (≥0.77 wt.%) and a copper content of up to 8.8 wt.%, the pearlitic transformation region

is significantly narrowed, and under rapid cooling conditions, pearlite formation is almost completely suppressed. This finding is consistent with that reported by Yi et al. [130].

Table 14. Summarised critical temperature data for the analysed deposited metals were obtained with self-shielded flux-cored wires of different compositions and hardfacing modes.

N/ Specimen	Filler Material	Fs	Ps	Bs	Martencite	
					Ms	Me
P3-E1-1	FCAW-P3-E1-1	767.1	516	764.1	301.6	181.5
P3-E1-2	FCAW-P3-E1-1	765.9	497.3	752.9	277.2	154.6
P3-E1-3	FCAW-P3-E1-1	767.3	497.6	753	272.0	148.8
P3-E1-4	FCAW-P3-E1-2	761.4	461.7	748	258.5	133.7
P3-E1-5	FCAW-P3-E1-2	754.8	454.2	734.9	227.5	98.9
P3-E1-6	FCAW-P3-E1-2	767.8	463.4	757.8	270.2	146.8
P3-E1-7	FCAW-P3-E1-3	775.4	477.2	767.1	269.2	145.7
P3-E1-8	FCAW-P3-E1-3	769.3	462.4	758.1	262.1	137.7
P3-E1-9	FCAW-P3-E1-3	766.9	457.4	748.3	224.8	95.8

Fs—start temperature of transformation of austenite into ferrite (more than 0.01% of volume); Ps—start temperature of transformation of austenite into pearlite (more than 0.01% of volume); Bs—start temperature of transformation of austenite into bainite (more than 0.01% of volume); Ms—temperature of the beginning of martensitic phase appearance from residual austenite (more than 0.01% of volume); Me—the temperature of the end of transformation of the residual austenitic phase to the martensitic phase (more than 90% of the volume).

For all investigated steels, the bainitic transformation region (Bs–Bf) is located within the range of intermediate temperatures and cooling times. For steels with increased carbon and copper content, earlier suppression of pearlite transformation and expansion of the temperature–time range of bainite and martensite formation were observed. An increase in copper content reduced the bainite transformation temperature. According to Table 14, alloy P3-E1-8, which has a high copper content of 8.6 wt.%, exhibits a significantly lower bainite transformation temperature than alloy P3-E1-1, which has a moderate copper content of 3.1 wt.%, despite having comparable levels of other alloying elements.

Analysis of the CCT diagrams reveals a significant and consistent combined impact of copper content and cooling rate on the microstructural evolution of the deposited metal. Copper stabilises undercooled austenite, a finding that is supported by previous studies [131]. In steels with an elevated copper content, the microstructure is dominated by fine bainite, with a limited fraction of martensite, even at moderate cooling rates of approximately CR = 43–45 °C·s^{-1} (Figure 16e–g). At the highest cooling rates (Figure 18a,i), copper's effect is evident in the reduction of the bainitic transformation temperature range and the increased formation of lower bainite and martensite from austenite [130].

Given the non-equilibrium nature of the cooling processes inherent in welding, thermodynamic simulations were performed to evaluate the evolution of the phase state under the influence of the specific thermal cycles [132]. The resulting calculated phase diagrams and the corresponding phase distribution within the deposited metal for the investigated samples are illustrated in Figure 19, reflecting the structural transformations as a function of the welding parameters.

Considering the conditions of the experiment (Figure 19a–i), namely cooling in air to a temperature of 200 °C, the phase composition of the sample matrix was determined at this temperature.

The results of thermodynamic modelling of phase transformations during the welding cycle showed that for all nine samples of deposited metal, an almost completely austenitic structure was formed in the temperature range above Ac_3. During subsequent accelerated cooling, diffusion transformations (ferrite–pearlite and bainite) were suppressed, and

martensite became the main product of austenite decomposition, accounting for more than 80–90 wt.% of the final structure for all compositions.

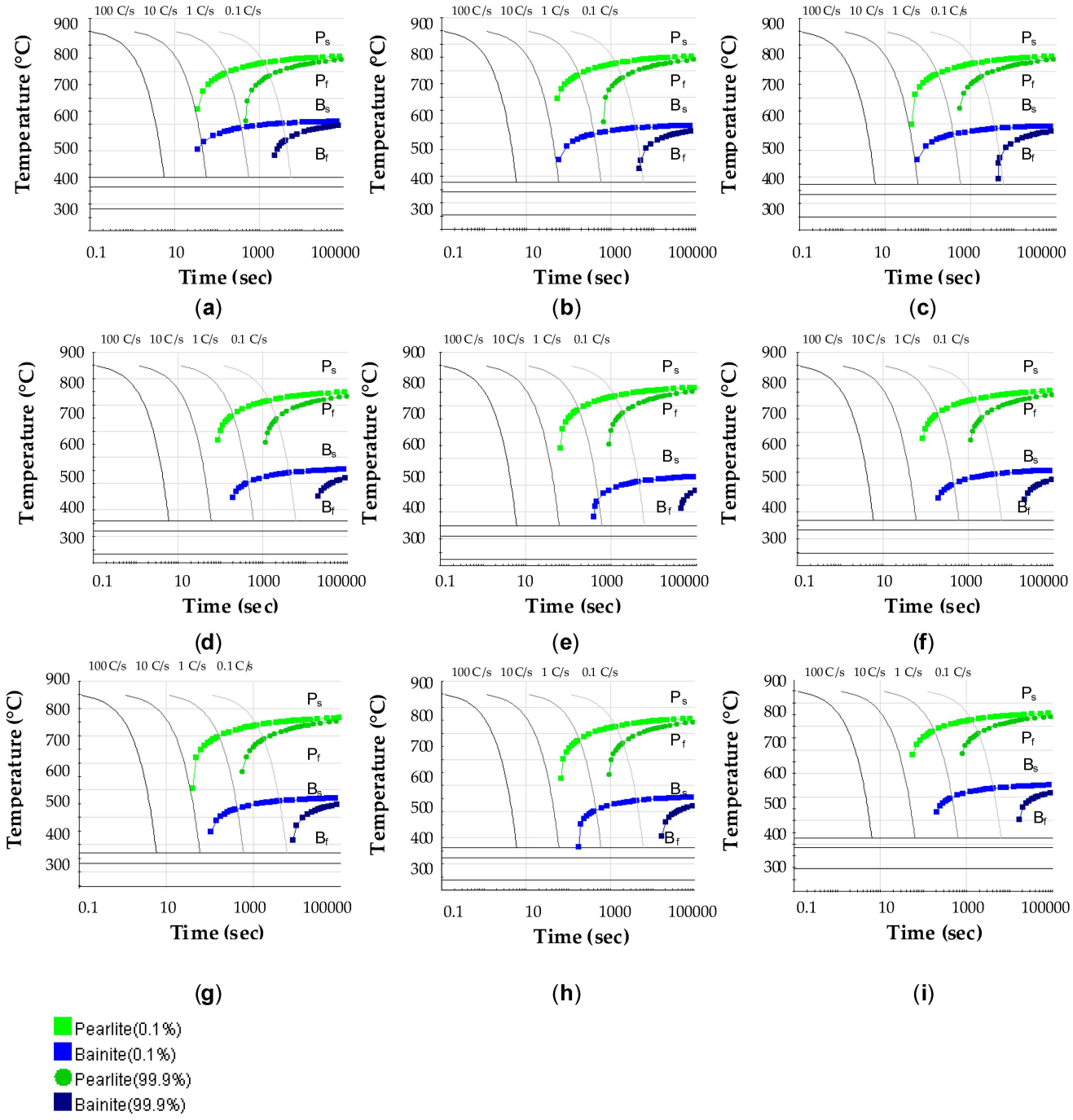

Figure 18. Continuous cooling transformation (CCT) diagrams of experimental materials constructed using JMatPro software (JMatPro, Release 7.0, Sente Software Ltd., Guildford, UK, 2016) during hardfacing for deposited metal samples: (**a**) P3-E1-1, (**b**) P3-E1-2, (**c**) P3-E1-3; (**d**) P3-E1-4, (**e**) P3-E1-5, (**f**) P3-E1-6; (**g**) P3-E1-7, (**h**) P3-E1-8, and (**i**) P3-E1-9.

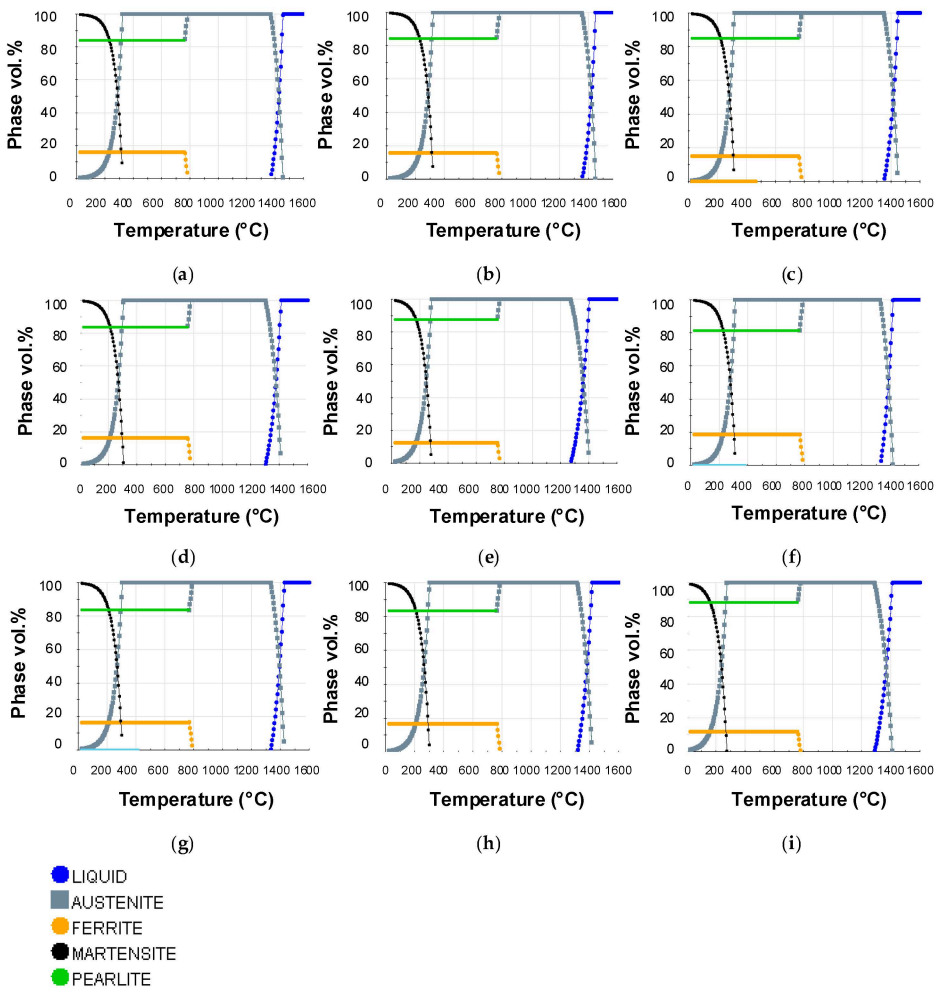

Figure 19. JMatPro simulation of phases during the welding cycle (rate of heating *RH* = 1000 °C/s, graine size 13 μm) for deposited metal (cooling rate see Table 8): (**a**) P3-E1-1; (**b**) P3-E1-2; (**c**) P3-E1-3; (**d**) P3-E1-4; (**e**) P3-E1-5; (**f**) P3-E1-6; (**g**) P3-E1-7; (**h**) P3-E1-8; and (**i**) P3-E1-9.

It was established that an increase in the carbon content in the deposited metal was the determining factor in the formation of a high-martensitic structure after the welding cycle: an increase in C concentration led to a decrease in the start temperature of martensitic transformation and an increase in hardenability. However, an increase in Cu concentration led to an expansion of the temperature range of austenite existence and a slight decrease in the start temperature of martensitic transformation, which contributed to the formation of a more dispersed martensitic matrix. Thus, the matrix of the deposited metal will consist of martensite.

3.5.2. Study of the Microstructure of the Deposited Metal

To confirm the theoretical results obtained, a sample of P3-E1-1 and P3-E1-7 metal was examined, which was produced for the worst experiment Exp.1 and studied under the optimal conditions of the experiment Exp.7. The microstructure of the hardfacing layer was observed by scanning electron microscopy using a ZEISS EVO 40XVPmicroscope, with an INCA Energy X-ray microanalysis system.

The SEM image of the microstructure confirmed that it consists of a tempered martensite matrix with eutectic. The microstructure exhibited a eutectic constituent localised at the dendritic margins, forming a continuous mesh (Figure 20a1,b1). This constituent was identified as a composite of austenite solid solution and $Cr_{23}C_7$carbides. The microstructural analysis of the Fe-C-Cr-Ti-Cu system reveals that increasing the copper content from

3.1 wt.% in sample P3-E1-1 to 7.5 wt.% in sample P3-E1-7 significantly influences the phase transformation kinetics and final constituent morphology. Thermodynamic simulations using JMatPro indicate that higher copper concentrations stabilise the austenite phase, resulting in a depression of the martensite start (M_s) temperature from 301.6 °C to 269.2 °C and the martensite finish (M_e) temperature from 181.5 °C to 145.7 °C. Equilibrium phase diagrams confirm that while both alloys form a matrix of ferrite and martensite reinforced by M7C3 carbides and M(C,N) carbonitrides. SEM observations at 2000× magnification correlate these findings, showing that while P3-E1-1 maintains a refined martensitic–ferritic structure with dispersed carbides, the P3-E1-7 sample displays a more heterogeneous morphology with distinct copper-rich inclusions and a modified carbide distribution, which are critical factors in the synergistic optimisation of elemental transfer efficiency and hardfacing performance.

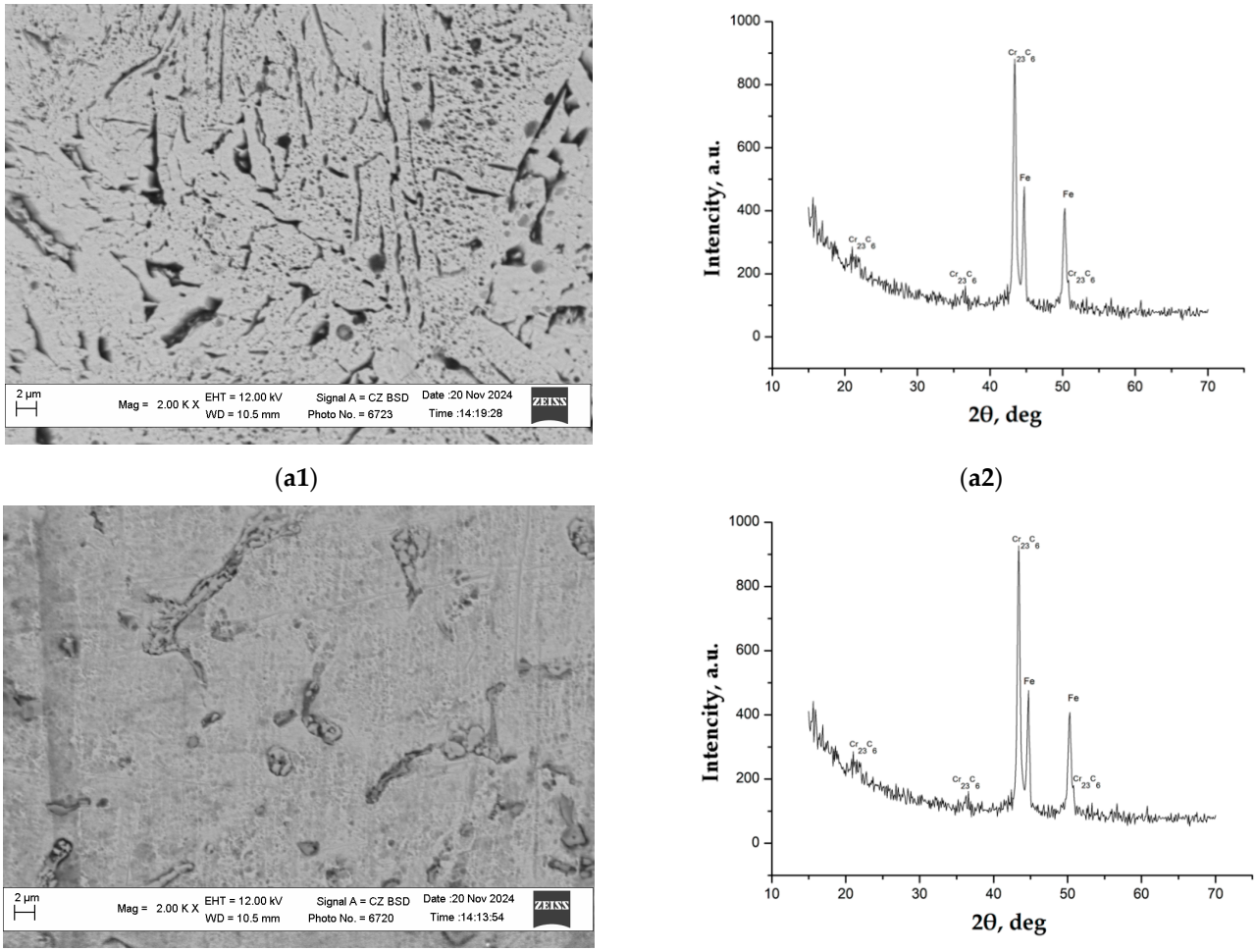

Figure 20. Microstructure and phase composition of the 50Cr3Cu7TiV alloy samples: SEM images (×2000) of (**a1**) sample P3-E1-1 and (**b1**) sample P3-E1-7; XRD patterns of (**a2**) sample P3-E1-1 and (**b2**) sample P3-E1-7.

The microstructural evolution during the entire cooling process (crystallisation and subsequent cooling in the solid state) of the Fe-C-Cr-Ti-Cu alloy system was shown schematically in Figure 21.

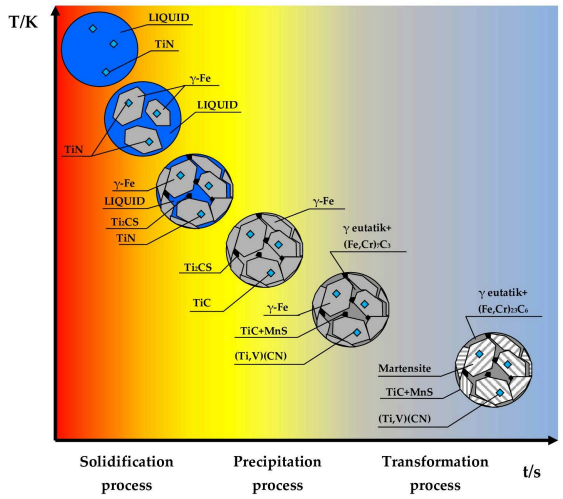

Figure 21. Scheme of microstructural evolution during solidification and subsequent solid-state cooling of deposited metal Fe-C-Cr-Ti-Cu alloy system.

3.6. Study of Exothermic Additions to the Chemical Composition of Slag

During the welding/surfacing process using self-shielded flux-cored wires, slag has a significant impact on their chemical composition [133]. Slag composition affects the gas content in the molten metal (such as nitrogen and oxygen) and inclusions dissolved during welding [134]. The introduction of an exothermic addition into the flux-cored wire filler changes the chemical composition of the slag. This is primarily due to the presence of an active reducing agent, Al powder. As a result of the exothermic reaction, a large amount of Al_2O_3 is formed, which changes the physicochemical properties of the slag. This is also confirmed by the results of studies by Li et al. [111]. This also caused a decrease in the basicity of the slag.

Table 15 shows the composition of slag with different Al/Fe_2O_3 content and deposited under different deposition conditions.

Table 15. The compositions of slag (wt.%).

№ Exp.	CaF_2	TiO_2	CaO	ZrO_2	MgO	MnO	SiO_2	Cr_2O_3	Al_2O_3	FeO	BI
1	22.66	23.48	4.84	5.42	0.35	7.13	5.05	16.62	12.92	1.53	0.94
2	24.41	25.72	5.21	5.84	0.38	5.45	7.40	10.62	13.59	1.39	0.95
3	23.15	23.89	4.94	5.54	0.36	6.55	6.84	14.71	12.71	1.31	0.92
4	28.09	24.37	6.00	6.72	0.43	2.38	0.62	2.68	27.33	1.38	1.17
5	28.36	26.44	6.05	6.78	0.44	1.12	1.53	0.66	27.22	1.39	1.13
6	26.58	21.61	5.67	6.36	0.41	3.74	1.25	8.35	24.73	1.30	1.11
7	22.77	21.16	4.86	6.54	0.39	3.83	0.87	10.39	28.70	0.49	0.88
8	24.46	19.87	5.22	7.02	0.42	1.29	1.92	7.82	31.44	0.52	0.89
9	24.79	23.69	5.29	7.12	0.43	0.33	4.70	3.42	29.70	0.53	0.84
min	22.66	19.87	4.84	5.42	0.35	0.33	0.62	0.66	12.71	0.49	0.84
max	28.36	26.44	6.05	7.12	0.44	7.13	7.40	16.62	31.44	1.53	1.17
Av	25.03	23.36	5.34	6.37	0.40	3.54	3.36	8.36	23.15	1.09	

The basic to acidic components ratio was known as the basicity index (BI) and was calculated by Equation (2) in mass% values [135,136].

$$BI = \frac{[\%CaF_2 + \%CaO + \%MgO + \%BaO + \%Na_2O + \%K_2O + \%Li_2O + 0.5\cdot(\%MnO + \%FeO)]}{[\%SiO_2 + 0.5\cdot(\%Al_2O_3 + \%TiO_2 + \%ZrO_2)]}, \quad (30)$$

The studied slag system can be classified as a multicomponent oxide–fluoride system: CaF_2-TiO_2-Al_2O_3-CaO-ZrO_2. Low MnO content (avg. 3.54%) indicates an exothermic reaction. BI varies in the range of 0.84–1.17, with an average value of 0.98. The slag is neutral or weakly basic. This ensures good bead formation and easy separability of the slag crust. In experiments four, five, and 6six an increase in BI (>1.1) is observed due to the high content of Al_2O_3 and CaF_2. Low content of iron oxides FeO (avg. 1.09%) indicates high deoxidation of the weld pool. In experiments one, two, and three, an increased content of Cr_2O_3 (up to 16.62%) is observed, which may indicate partial loss of chromium. With an increase in the *EA* content from 18 wt.% to 28 wt.%, the reducing capacity of the slag increased. The Al_2O_3 content increased from ~13% to ~26%. A further increase in EA does not lead to a significant increase in the Al_2O_3 content. The high Al_2O_3 content in experiments four to nine indicates the introduction of a higher percentage of the exothermic mixture.

According to Coetsee [136], the decrease in chromium and manganese oxidation is facilitated by increasing slag basicity (which decreases the activity of oxides). The research results showed that for the process performed with flux-cored wire, the FCAW-P3-E1-1 and FCAW-P3-E1-3 indexes (*EA* = 18 wt.% and *EA* = 38 wt.%), the average value of chromium transfer was $\eta(Cr) = 0.703$ and $\eta(Cr) = 0.818$, respectively (Figure 22). Whereas the processes performed with FCAW P3 E1 2 a basic slag, $\eta(Cr) = 0.931$ (Figure 22). The results also indicate that an increase in the Al_2O_3 content in the slag crusts had a positive effect on the transfer coefficients of silicon, manganese, and titanium, which is consistent with the results of the studies of Bang et al. [137]. Some decrease in the conversion factors when moving from flux-cored wire with medium to high EA content, characterised by an increase in Al_2O_3 content, can be associated an increase in viscosity and density [138]. This can lead to losses due to sticking of unmelted particles in the slag.

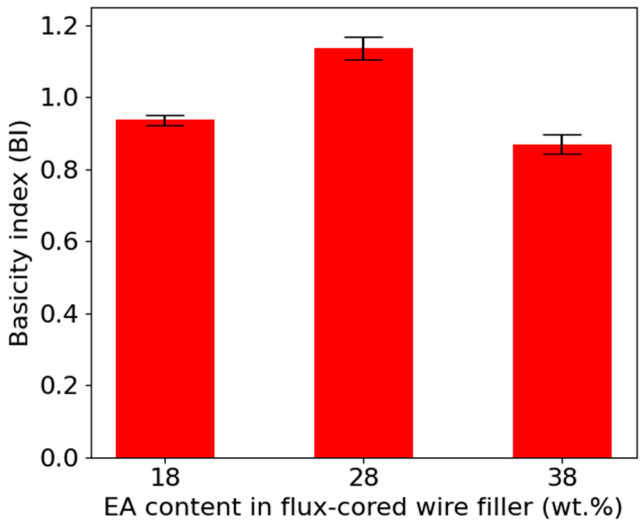

Figure 22. Effect of exothermic addition content (CuO + Al) in the flux-cored wire filler on the flux basicity.

4. Discussion

The analysis showed a significant influence of the amount of CuO-Al exothermic addition on the transition of alloying elements. At the same time, according to the influence of welding parameters, the transition coefficients of elements could be grouped into three groups: deoxidisers (aluminium, silicon and manganese), carbide-forming elements with carbon (chromium, vanadium, titanium and carbon), and the reducible element of the exothermic addition. For the transition of elements in the deoxidiser group, along with

the strong influence of *EA*, the second most important parameter was the *CTWD*. High transition values $\eta(Al)$, $\eta(Si)$ and $\eta(Mn)$ were achieved at low contact tip-to-work distance values *CTWD* = 35 mm and medium or high *EA* content 30–40 wt.%.

The transition of carbide-forming elements such as carbon and vanadium was most influenced by parameters related to the melting of the filler material, namely the wire feed speed (*WFS*) and the voltage set on the power source (U_{set}), which determined the power of the welding arc. The percentage of exothermic addition in the core filler and the associated contact tip-to-work distance determined the amount of heat generated by the chemical reaction. The optimal values at which the highest values of $\eta(C)$ and $\eta(V)$ were achieved: *WFS* = 1.85 m·min^{-1} (medium level), U_{set} = 28 V (low level), *EA* = 30 wt.% (medium level). Low voltage values could be explained by air suction [139] and an increase in the length of the electrode extension section [106]. The positive effect of the exothermic addition was associated with improved uniformity of flux-cored wire melting. At the same time, diffusion dissolution of graphite into droplets of molten metal at the electrode tip was observed. This was also confirmed by the results of studies by Zhudra et al. [102]. In the case of a significant effect of uneven melting of the filler and metal shell, undissolved graphite particles may enter the weld pool. Low carbon transfer was caused by graphite entering the weld pool in an unmelted state due to the collapse of the flux column. Graphite granules that did not have time to react completely at the droplet and weld pool stages floated up (due to their low specific weight) and were transferred into the slag [102]. Carbon losses, when the filler had a high exothermic addition content, may be caused by its oxidation as a result of the carbothermic reaction $2CuO + C \rightarrow 2Cu + CO_2\uparrow$ [92,140]. In addition, the melting of the core filler and its transition into a drop of molten metal, followed by heating at the droplet stage, promoted the dissolution and transition into the liquid metal solution of carbide-forming elements such as Cr, V, and Ti. This prevented their burnout due to interaction with the air. Burnout will also be facilitated by an increase in voltage, i.e., the associated arc length.

When melting in the charge, carbon binds with carbide-forming elements (chromium, vanadium, etc.) to form refractory compounds [92]. In a bound state, it is transferred into a molten metal droplet, thus preventing the burnout of elements such as V. Meanwhile, titanium Ti will bind into titanium nitride at high temperatures, as confirmed by thermodynamic calculations. The significant influence of welding current and arc voltage on the transition of C and Cr was also reported in the study by Garg et al. [141]. However, the determining variable influencing the overall transition coefficient of alloying elements was *EA*. This indicated a positive influence.

The analysis of the influence of variables on the parameters of the welding thermal cycle and hardness showed a dependence on *WFS* and U_{set}. This could be explained by their influence on the arc power. It was known that when welding/surfacing with self-shielded flux-cored wires, the welding current was primarily determined by the wire feed speed [124]. The influence of *EA* was not so noticeable, but the early occurrence of exothermic reactions could lead to a decrease in welding current caused by the melting of the core filler [114]. Thus, the amount of exothermic addition introduced had a significant effect on the transition of elements, as well as a slight effect on the parameters of the welding thermal cycle. The analysis showed that the microstructure will depend on the composition of the deposited metal. Changes in the chemical composition of the deposited metal and the cooling rate had a significant effect on the microstructure, phase composition, and mechanical properties of the deposited metal. An increase in the content of Cr and Cu significantly shifted the curves of the start of pearlite formation towards longer durations and lower temperatures. The latter indicated an increase in hardenability [130,142]. At high copper content (6–8 wt.%), an increase in carbon content from 0.55 wt.% to 0.77 wt.%

led to complete suppression of pearlite formation. Copper acted as a potent stabiliser of supercooled austenite [131]. Higher Cu concentrations led to a distinct depression of the bainite start temperature. Specifically, alloy P3-E1-8 (8.6 wt.% Cu) demonstrated a significantly lower transformation temperature compared to alloy P3-E1-1 (3.1 wt.% Cu), confirming the role of copper in refining the transformation products. The main alloying elements that determined the microstructure of the matrix and the content of the strengthening phase in the form of carbides were carbon and chromium [143]. Cr_7C_3 carbides were formed at $Cr/C \geq 2$, and $Cr_{23}C_6$ carbides were formed at $Cr/C \geq 5$. The results of our studies showed that the formation of $Cr_{23}C_6$ carbides in Fe-C-Cr-Ti-Cu alloys was observed at Cr/C ratios ≥ 4.7. The formation of orthogonal carbide Cr_7C_3 was preferable to that of orthogonal carbide $Cr_{23}C_6$, which had a lower calculated microhardness (HV = 13.5 GPa versus HV = 10.1 GPa [144]).

Analysis of the obtained hardness values showed (Table 8) that the highest hardness was exhibited by alloys P3-E1-8 and P3-E1-2 (752.3 HV and 613 HV, respectively). Their microstructure corresponded to martensitic. These alloys contained C = 0.52–0.57 wt.% and had a Cr/C ratio of 5.19–5.27. For alloys P3-E1-1, P3-E1-3, P3-E1-6, and P3-E1-7 with a tempered martensite structure, their hardness ranged from HV = 535 to 569. The lowest hardness was observed in alloys with indices P3-E1-4, P3-E1-5 and P3-E1-9, whose microstructure corresponded to the troostite structure with a hardness in the range of 400–500. The latter alloys had a high carbon content (C > 0.71) and chromium content (Cr = 3.9).

In view of the considerable interest in researching the influence of filler composition [145,146], methods for studying and controlling deposited metal [147,148], and increasing productivity [124], the proposed research methodology could be useful for optimising processes [149–151], developing and testing new materials and mechanical properties, modern technologies [152,153], and life cycle analysis [154–156].

5. Conclusions

The obtained results can be used to optimise surfacing parameters, improve the compositions of flux-cored wires, and predict the properties of the deposited layers. The statistical and experimental analysis of the surfacing process parameters yielded the following conclusions regarding the transfer coefficients of alloying elements:

1. Based on their response to welding parameters, the alloying elements could be categorised into three distinct groups: deoxidisers (Al, Si, and Mn), carbide-forming elements (Cr, V, Ti, and C), and the recovery element from the exothermic addition (Cu).
2. The transfer coefficients such deoxidisers as$\eta(Al)$, $\eta(Si)$, and $\eta(Mn)$ were primarily governed by the percentage of exothermic addition (EA) and the contact tip-to-work distance ($CTWD$). High values of their conversion coefficients are achieved at EA = 28 wt.% and $CTWD$ = 35 mm.
3. The transfer coefficients $\eta(C)$ and $\eta(V)$ were highly sensitive to parameters affecting the filler material melting and arc power—specifically wire feed speed (WFS) and voltage (U_{set}). Optimal transition for $\eta(C)$ and $\eta(V)$ was observed at WFS = 1.85 m·min^{-1} (medium level), U_{set} = 28 V (low level), and EA = 28 wt.%.
4. Maximum recovery was achieved at low contact tip-to-work distance ($CTWD$ = 35 mm) and medium-to-high EA content (EA = 38 wt.%,).
5. It was established that copper had a pronounced stabilising effect on supercooled austenite in Fe–C–Cr–Cu steels, shifting the 'nose' of pearlite transformation to longer times and lower temperatures. This, in turn, expanded the time–temperature range for bainite transformation. Copper at high concentrations (≥7 wt.%) further stabilised austenite and promoted increased hardenability.

6. High-copper Fe–C–Cr–Cu steels, with increasing carbon and chromium content, exhibited a narrower austenite region. Increased copper content contributed to the expansion of the austenite stability range and shifted the γ-phase region toward lower temperatures.
7. The highest hardness values (613–752.3 HV) were achieved in alloys with a martensitic microstructure, characterised by C = 0.52–0.57 wt.% and a Cr/C > 5.2. Alloys with higher carbon (C > 0.71) and lower chromium (Cr/C = 4–4.7) exhibited a troostite structure with lower hardness (400–500 HV).
8. The study successfully implemented an advanced synergistic Taguchi–ANOVA–FD–PCA–GRA approach, a combined Taguchi-ANOVA-based approach with a hybrid Taguchi–GRA–PCA methodology for an orthogonal four-factor, three-level experimental design. This integrated approach facilitated the systematic identification and exclusion of insignificant variables through ANOVA to develop mathematical models using FD while effectively addressing multi-objective optimisation challenges.
9. Optimal values of the studied variables were obtained for the multi-objective problem using the hybrid Taguchi–GRA–PCA methodology. The optimal parameters identified are as follows: *EA* = 38 wt.%, *CTWD* = 35 mm, *WFS* = 2.07 m min^{-1}, and U_{set} = 31 V, which ensures high process productivity, minimal spatter, high hardness, and alloying element transition.

Author Contributions: Conceptualisation, B.T.; methodology, B.T. and M.K.; software, B.T. and M.K.; validation, Y.K. and I.P.; formal analysis, L.N.; investigation, B.T.; resources, B.T. and M.K.; data curation, I.P. and M.K.; writing—original draft preparation, B.T.; writing—review and editing, L.N., O.I., and B.H.; visualisation, M.K. and B.T.; supervision, I.T., Y.K., and L.N.; project administration, B.T.; funding acquisition, B.T., M.K., and L.N. All authors have read and agreed to the published version of the manuscript.

Funding: This research received no external funding.

Institutional Review Board Statement: Not applicable.

Informed Consent Statement: Not applicable.

Data Availability Statement: The original contributions presented in this study are included in the article. Further inquiries can be directed to the corresponding author.

Conflicts of Interest: Author Bohdan Trembach was employed by the Private Joint Stock Company "Novokramatorsky Mashinostroitelny Zavod". The remaining authors declare that the research was conducted in the absence of any commercial or financial relationships that could be construed as a potential conflict of interest.

Abbreviations

The following abbreviations are used in this manuscript:

GRA	Grey Relational Analysis
PCA	Principal Component Analysis
ANOVA	Analysis of Variance
RSM	Response Surface Methodology
FCAW	Flux-Cored Arc Welding
WFS	Wire Feed Speed
CTWD	Contact Tip-to-Work Distance
EA	Percentage of exothermic mixture in the core filler
MOR	Melting-Off Rate
DR	Deposition Rate
SF	Spattering Factor

De	Deposition Efficiency
R sqr	Coefficient of Determination
R Adj	Adjusted Sum of Squares
$RE(Cu)$	Copper Recovery Factor
$\eta(E)$	Element Transfer coefficient (where E is C, Cr, Si, Mn, Al, Ti, V)
HI	Heat Input
TS	Travel Speed
η_{FCAW}	Coefficient of Efficiency of the Process
CR	Cooling Rate
$\Delta t_{8/5}$	Cooling Time
λ	Material Thermal Conductivity

References

1. Bala, Y.G.; Rajendran, D.K. Global Welding Market Growth. In *Automation in Welding Industry: Incorporating Artificial Intelligence, Machine Learning and Other Technologies*; Wiley: Hoboken, NJ, USA, 2024; pp. 229–243. [CrossRef]
2. Trembach, B.; Starikov, V.; Sukov, M.G.; Zharikov, S.; Kabatskyi, O.; Ivanova, Y. Application of Mixture design in optimization of physical properties of slag during self-shielded flux-cored wire arc welding process. In Proceedings of the IEEE 5th International Conference on Modern Electrical and Energy System, MEES 2023, Kremenchuk, Ukraine, 27–30 September 2023; pp. 1–5.
3. Trembach, B. Comparative studies of the three-body abrasion wear resistance of hardfacing Fe-Cr-C-B-Ti alloy. *Proc. IOP Conf. Ser. Mater. Sci. Eng.* **2023**, *1277*, 012016. [CrossRef]
4. Liu, Q.; Mi, H.; Feng, L.; Guo, W.; He, B. A critical overview of welding and directed energy deposition with flux-cored wires. *J. Manuf. Process.* **2025**, *142*, 231–268. [CrossRef]
5. Magalhães, K.M.M.; Brasil, R.M.L.R.F.; Wahrhaftig, A.M.; Siqueira, G.H.; Bondarenko, I.; Neduzha, L. Influence of Atmospheric Humidity on the Critical Buckling Load of Reinforced Concrete Columns. *Int. J. Struct. Stab. Dyn.* **2022**, *22*, 2250011. [CrossRef]
6. Myamlin, S.; Neduzha, L.; Urbutis, Ž. Research of Innovations of Diesel Locomotives and Bogies. *Procedia Eng.* **2016**, *134*, 470–475. [CrossRef]
7. Myamlin, S.; Lunys, O.; Neduzha, L.; Kyryl'chuk, O. Mathematical modeling of dynamic loading of cassette bearings for freight cars. In Proceedings of the 21st International Scientific Conference Transport Means, Juodkrante, Lithuania, 20–22 September 2017; pp. 973–976.
8. Bondarenko, I.; Lukoševičius, V.; Keršys, R.; Neduzha, L. Investigation of Dynamic Processes of Rolling Stock–Track Interaction: Experimental Realization. *Sustainability* **2023**, *15*, 5356. [CrossRef]
9. Sawczuk, W.; Jüngst, M.; Ulbrich, D.; Kowalczyk, J. Modeling the Depth of Surface Cracks in Brake Disc. *Materials* **2021**, *14*, 3890. [CrossRef] [PubMed]
10. Ulbrich, D.; Kowalczyk, J.; Stachowiak, A.; Sawczuk, W.; Selech, J. The Influence of Surface Preparation of the Steel during the Renovation of the Car Body on Its Corrosion Resistance. *Coatings* **2021**, *11*, 384. [CrossRef]
11. Ning, Y.; Qiu, Z.; Wu, B.; Pan, Z.; Li, H. Hardfacing of metals: A review of consumables, properties and strengthening processes. *J. Mater. Res. Technol.* **2025**, *36*, 6330–6349. [CrossRef]
12. Singla, Y.K.; Maughan, M.R.; Arora, N.; Dwivedi, D.K. Enhancing the Wear Resistance of Iron-Based Alloys: A Comprehensive Review of Alloying Element Effects. *J. Manuf. Process.* **2024**, *120*, 135–160. [CrossRef]
13. Zurnadzhy, V.; Stavrovskaia, V.; Chabak, Y.; Petryshynets, I.; Efremenko, B.; Wu, K.; Efremenko, V.; Brykov, M. Enhancing the Tensile Properties and Ductile-Brittle Transition Behavior of the EN S355 Grade Rolled Steel via Cost-Saving Processing Routes. *Materials* **2024**, *17*, 1958. [CrossRef]
14. Czapiewski, W.; Pałubicki, S.; Plichta, J.; Nadolny, K. State of Knowledge in the Field of Regenerative Hardfacing Methods in the Context of the Circular Economy. *Appl. Sci.* **2026**, *16*, 792. [CrossRef]
15. Zhou, B.; Wu, Y.; Zheng, H. Investigation of Electrochemical Assisted Deposition of Sol-Gel Silica Films for Long-Lasting Superhydrophobicity. *Materials* **2023**, *16*, 1417. [CrossRef] [PubMed]
16. Lin, Z.; Li, X.; Chen, G.; Cao, Y.; Ren, L.; Shao, H.; Zhao, X. A review of material surface processing utilizing gas cluster ion beam technology. *Eur. Phys. J. D* **2025**, *79*, 50. [CrossRef]
17. Hvozdetskyi, V.M.; Student, M.M.; Zadorozhna, K.R.; Veselivska, H.H.; Markovych, S.I.; Mozola, N.Z. Mechanical characteristics of electric arc coatings sputtered on St3 steel and D16 aluminum alloy. *Mater. Sci.* **2025**, *61*, 147–155. [CrossRef]
18. Luk'yanenko, A.G.; Hvozdetskyi, V.M.; Student, M.M.; Student, O.Z.; Lavrys, S.M.; Mozola, N.Z. Thermodynamic analysis of the formation of chemical compounds reactions during arc spraying of coatings with cored wires. *Mater. Sci.* **2024**, *60*, 283–290. [CrossRef]

19. Hlushkova, D.B.; Bagrov, V.A.; Demchenko, S.V.; Volchuk, V.M.; Kalinin, O.V.; Kalinina, N.E. Structure and properties of powder gas-plasma coatings based on nickel. *Probl. At. Sci. Technol.* **2022**, *140*, 125–130. [CrossRef]
20. Vahrusheva, V.S.; Hlushkova, D.B.; Volchuk, V.M.; Nosova, T.V.; Mamhur, S.I.; Tsokur, N.I.; Bagrov, V.A.; Demchenko, S.V.; Ryzhkov, Y.V.; Scrypnikov, V.O. Increasing the corrosion resistance of heat-resistant alloys for parts of power equipment. *At. Sci. Technol.* **2022**, *140*, 137–140. [CrossRef]
21. Efremenko, V.G.; Chabak, Y.G.; Lekatou, A.; Karantzalis, A.E.; Shimizu, K.; Fedun, V.I.; Azarkhov, A.Y.; Efremenko, A.V. Pulsed plasma deposition of Fe-C-Cr-W coating on high-Cr-cast iron: Effect of layered morphology and heat treatment on the microstructure and hardness. *Surf. Coat. Technol.* **2016**, *304*, 293–305. [CrossRef]
22. Efremenko, V.G.; Chabak, Y.G.; Fedun, V.I.; Shimizu, K.; Pastukhova, T.V.; Petryshynets, I.; Zusin, A.M.; Kudinova, E.V.; Efremenko, B.V. Formation mechanism, microstructural features and dry-sliding behaviour of "Bronze/WC carbide" composite synthesised by atmospheric pulsed-plasma deposition. *Vacuum* **2021**, *185*, 110031. [CrossRef]
23. Tkachuk, O.V.; Hvozdetskyi, V.M.; Student, M.M.; Zadorozhna, K.R.; Kovalchuk, I.V.; Pohrelyuk, I.M. Structural features and wear resistance of the TiAlN coating on the Ti–6Al–4V alloy formed by combining electric arc spraying and gas nitriding methods. *Mater. Sci.* **2025**, *60*, 453–461. [CrossRef]
24. Hvozdetskyi, V.M.; Student, O.Z.; Student, M.M.; Pokhrelyuk, I.M.; Zadorozna, K.R.; Lukyanenko, A.G. Physicomechanical properties of arc sprayed coating formed in supersonic mode. *Mater. Sci.* **2024**, *60*, 189–197. [CrossRef]
25. Hvozdets'kyi, V.; Padgurskas, J.; Student, M.; Pohrelyuk, I.; Student, O.; Zadorozhna, K.; Tkachuk, O.; Rukuiža, R. The tribological properties of plasma electrolytic oxidation layers synthesized on arc spray coatings on aluminum alloys in contact with various friction materials. *Coatings* **2024**, *14*, 460. [CrossRef]
26. Chabak, Y.; Efremenko, V.; Barma, Y.; Petrišinec, I.; Efremenko, B.; Kromka, F.; Sili, I.; Kovbasiuk, T. Enhancing Dry-Sliding Wear Performance of a Powder-Metallurgy-Processed "Metal Matrix–Carbide" Composite via Laser Surface Modification. *Eng* **2025**, *6*, 313. [CrossRef]
27. Efremenko, B.V.; Zurnadzhy, V.I.; Chabak, Y.G.; Efremenko, V.G.; Kudinova, K.V.; Mazur, V.A. A comparison study on the effect of counter ball material on sliding wear response of SLM-printed biomedical 316L steel. *Mater. Today Proc.* **2022**, *66*, 2587–2593. [CrossRef]
28. Duriagina, Z.; Kulyk, V.; Kovbasiuk, T.; Vasyliv, B.; Kostryzhev, A. Synthesis of functional surface layers on stainless steels by laser alloying. *Metals* **2021**, *11*, 434. [CrossRef]
29. Tandon, D.; Li, H.; Pan, Z.; Yu, D.; Pang, W. A Review on Hardfacing, Process Variables, Challenges, and Future Works. *Metals* **2023**, *13*, 1512. [CrossRef]
30. Mishra, S.; Sharma, L.; Chhibber, R. Contact angle measurement for SMAW electrode coating fluxes: Effect of electrode coating flux compositions on different wetting parameters using statistical models. *Int. J. Interact. Des. Manuf.* **2025**, *19*, 5621–5640. [CrossRef]
31. Gupta, A.; Singh, J.; Chhibber, R.; Singla, Y.K. Quantitative analysis of thermal properties in SMAW electrode coatings based on CaF_2-Al_2O_3-CaO-SiO_2 using regression models. *Int. J. Adv. Manuf. Technol.* **2025**, *140*, 1731–1747. [CrossRef]
32. Coetsee, T.; De Bruin, F. Sodium-Oxide Fluxed Aluminothermic Reduction of Manganese Ore for a Circular Economy: Cr Collector Metal Application. *Sustain. Chem.* **2025**, *6*, 30. [CrossRef]
33. Vlasov, A.F.; Makarenko, N.A. Special features of heating and melting electrodes with an exothermic mixture in the coating. *Weld. Int.* **2016**, *30*, 717–722. [CrossRef]
34. Silva, R.H.G.; dos Santos Paes, L.E.; Marques, C.; Riffel, K.C.; Schwedersky, M.B. Performing higher speeds with dynamic feeding gas tungsten arc welding (GTAW) for pipeline applications. *J. Braz. Soc. Mech. Sci. Eng.* **2019**, *41*, 38. [CrossRef]
35. Kumar, S.; Das, A.K. Wear resistance and hardness properties of TiB2–Fe coating developed on AISI 1020 steel by tungsten inert gas (TIG) cladding. *Ceram. Int.* **2022**, *48*, 30052–30065. [CrossRef]
36. Maurya, A.K.; Kumar, N.; Pandey, C.; Chhibber, R. Structure–property relationship assessment of dissimilar gas tungsten arc welded joint of pipeline steel and super duplex stainless steel for marine applications. *Arch. Civ. Mech. Eng.* **2024**, *24*, 164. [CrossRef]
37. Tisov, O.; Pashechko, M.; Yurchuk, A.; Chocyk, D.; Zubrzycki, J.; Prus, A.; Wlazło-Ćwiklińska, M. Microstructure and Friction Response of a Novel Eutectic Alloy Based on the Fe-C-Mn-B System. *Materials* **2022**, *15*, 9031. [CrossRef] [PubMed]
38. Tomaszewicz, D.; Chmielewski, P.; Hlushkova, D.B.; Volchuk, V.M.; Bagrov, V.A.; Saienko, V.O. Resource-efficient double-gas-shielded welding of alloy steeks: Effect of modes on structure and mechanical properties. *Probl. At. Sci. Technol.* **2026**, *1*, 134–139. [CrossRef]
39. Kornienko, A.N.; Makarenko, N.A.; Granovskij, A.V.; Kondrashov, K.A. Universal source for plasma-MIG surfacing and welding. *Svarochnoe Proizv.* **2001**, *9*, 25–26.
40. Chigarev, V.V.; Makarenko, N.A.; Kondrashov, K.A.; Voropaj, N.M. Peculiarities of melting of electrode wire in surfacing by the plasma-MIG method. *Avtomat. Svarka* **2001**, *8*, 12–15.

41. Zhu, Z.; Ran, M.; Li, X.; Ma, P.; Liu, S.; Wang, J. Microstructure and Hardness Characteristics of Swing-Arc SAW Hardfacing Layers. *Materials* **2024**, *17*, 2310. [CrossRef]
42. Coetsee, T.; De Bruin, F. A Review of the Thermochemical Behaviour of Fluxes in Submerged Arc Welding: Modelling of Gas Phase Reactions. *Processes* **2023**, *11*, 658. [CrossRef]
43. Coetsee, T.; De Bruin, F. Modification of Flux Oxygen Behaviour via Co-Cr-Al Unconstrained Metal Powder Additions in Submerged Arc Welding: Gas Phase Thermodynamics and 3D Slag SEM Evidence. *Processes* **2022**, *10*, 2452. [CrossRef]
44. Ma, Y.; Zhang, J.; Yu, Z.; Li, M.; Cai, Z.; Feng, D.; Ren, S.; Zheng, W.; Yang, J. Influence of Overlay Welding Process on the Morphology, Microstructure, and Performance of the Overlay Layer. *Metals* **2025**, *15*, 987. [CrossRef]
45. Ates, S.; Aslan, O.; Tümer, M.; Arisoy, C.F. Impact sliding wear behavior of Stellite 6 and Stellite 12 hardfacings. *Mater. Chem. Phys.* **2024**, *313*, 128762. [CrossRef]
46. Vlasov, A.F.; Makarenko, N.A.; Kushchiy, A.M. Using exothermic mixtures in manual arc welding and electroslag processes. *Weld. Int.* **2017**, *31*, 565–570. [CrossRef]
47. Lozynskyi, V.; Trembach, B.; Hossain, M.M.; Kabir, M.H.; Silchenko, Y.; Krbata, M.; Sadovyi, K.; Kolomiitse, O.; Ropyak, L. Prediction of phase composition and mechanical properties Fe–Cr–C–B–Ti–Cu hardfacing alloys: Modeling and experimental validations. *Heliyon* **2024**, *10*, e25199. [CrossRef]
48. Bembenek, M.; Prysyazhnyuk, P.; Shihab, T.; Machnik, R.; Ivanov, O.; Ropyak, L. Microstructure and Wear Characterization of the Fe-Mo-B-C—Based Hardfacing Alloys Deposited by Flux-Cored Arc Welding. *Materials* **2022**, *15*, 5074. [CrossRef] [PubMed]
49. Boiko, I.A.; Grin', A.G. Effect of the surface condition of fluxed-cored wires on the stability of the arc process. *Weld. Int.* **2015**, *29*, 543–547. [CrossRef]
50. Júnior, J.G.F.; Cardoso, A.H.C.; Bracarense, A.Q. Effects of TiC formation in situ by applying titanium chips and other ingredients as a flux of tubular wire. *J. Braz. Soc. Mech. Sci. Eng.* **2020**, *42*, 375. [CrossRef]
51. Prysyazhnyuk, P.; Biały, W.; Bembenek, M.; Panchuk, V.; Medvid, I.; Duriagina, Z.; Romanyshyn, T.; Vytvytskyi, V. Improving Ballistic Resistance of Armor Steel by FCAW with Hardfacing Alloys of Fe–Mo–Mn–B–C System. *Manag. Syst. Prod. Eng.* **2025**, *33*, 380–387. [CrossRef]
52. Świerczyńska, A.; Varbai, B.; Pandey, C.; Fydrych, D. Exploring the trends in flux-cored arc welding: Scientometric analysis approach. *Int. J. Adv. Manuf. Technol.* **2024**, *130*, 87–110. [CrossRef]
53. Wolski, A.; Świerczyńska, A.; Lentka, G.; Fydrych, D. Storage of high-strength steel flux-cored welding wires in urbanized areas. *Int. J. Precis. Eng. Manuf.-Green. Technol.* **2024**, *11*, 55–70. [CrossRef]
54. Holly, S.; Mayer, P.; Bernhard, C.; Posch, G. Slag characterisation of 308L-type stainless steel rutile flux-cored wires. *Weld. World* **2019**, *63*, 293–311. [CrossRef]
55. Mohamat, S.A.; Ibrahim, I.A.; Amir, A.; Ghalib, A. The effect of Flux Core Arc Welding (FCAW) processes on different parameters. In *Procedia Engineering*; Elsevier Ltd.: Amsterdam, The Netherlands, 2012; pp. 1497–1501. [CrossRef]
56. Routray, S.; Swain, R.; Mohapatro, R.N. Toward a Greener Weld for Integrating Sustainability into Welding Practices. In *Advanced Welding Technologies*; Wiley: Hoboken, NJ, USA, 2025; pp. 447–476. [CrossRef]
57. Szymura, M.; Czupryński, A.; Ochodek, V. Development of a Mathematical Model of the Self-Shielded Flux-Cored Arc Surfacing Process for the Determination of Deposition Rate. *Materials* **2024**, *17*, 5616. [CrossRef]
58. Brezinová, J.; Draganovská, D.; Guzanová, A.; Balog, P.; Viňáš, J. Influence of the Hardfacing Welds Structure on Their Wear Resistance. *Metals* **2016**, *6*, 36. [CrossRef]
59. Romek, D.; Ulbrich, D.; Selech, J.; Kowalczyk, J.; Wlad, R. Assessment of Padding Elements Wear of Belt Conveyors Working in Combination of Rubber–Quartz–Metal Condition. *Materials* **2021**, *14*, 4323. [CrossRef] [PubMed]
60. Yanchuk, V.; Kruhlov, I.; Zakiev, V.; Lozova, A.; Trembach, B.; Orlov, A.; Voloshko, S. Thermal and ion treatment effect on nanoscale thin films scratch resistance. *Metallofiz. Noveish. Tekhnol.* **2022**, *44*, 1275–1292. [CrossRef]
61. Kytsy, A.R.; Bazylyak, L.I.; Zirka, A.L.; Zavadsky, D.S.; Zibin, S.D.; Pilyuk, Y.V.; Vynar, V.A.; Podhurska, V.Y.; Zavaliy, I.Y. Nickel-containing composite material for electromagnetic radiation shielding. *Mater. Sci.* **2025**, *61*, 232–240. [CrossRef]
62. Świetlicki, A.; Walczak, M.; Szala, M.; Nowak, W.J.; Chocyk, D. Effect of the shot peening finishing on cavitation erosion and corrosion resistance of DMLS manufactured 17-4PH steel. *Eng. Fail. Anal.* **2025**, *182*, 110127. [CrossRef]
63. Trembach, B.O.; Sukov, M.G.; Vynar, V.A.; Trembach, I.O.; Subbotina, V.V.; Rebrov, O.Y.; Rebrova, O.M.; Zakiev, V.I. Effect of incomplete replacement of Cr for Cu in the deposited alloy of Fe–C–Cr–B–Ti alloying system with a medium boron content (0.5% wt.) on its corrosion resistance. *Metallofiz. Noveish. Tekhnol.* **2022**, *144*, 493–513. [CrossRef]
64. Prysyazhnyuk, P.; Bembenek, M.; Drach, I.; Korzhov, A.; Romanyshyn, L.; Ropyak, L. Restoration of the Impact Crusher Rotor Using FCAW with High-Manganese Steel Reinforced by Complex Carbides. *Manag. Syst. Prod. Eng.* **2024**, *32*, 294–302. [CrossRef]
65. Hlushkova, D.B.; Bagrov, V.A.; Saenko, V.A.; Volchuk, V.M.; Kalinin, A.V.; Kalinina, N.E. Study of wear of the bulding-up zone of martensite-austenitic and secondery hardening steels of the Cr-Mn-Ti system. *Probl. At. Sci. Technol.* **2023**, *144*, 105–109. [CrossRef]

66. Szala, M.; Walczak, M. Metallic and Ceramic Materials Integrity—Surface Engineering for Wear, Corrosion and Erosion Prevention. *Materials* **2024**, *17*, 1541. [CrossRef]
67. Wieczorek, D.; Ulbrich, D.; Stachowiak, A.; Bartkowski, D.; Bartkowska, A.; Petru, J.; Hajnyš, J.; Popielarski, P. Mechanical, corrosion and tribocorrosion resistance of additively manufactured Maraging C300 steel. *Tribol. Int.* **2024**, *195*, 109604. [CrossRef]
68. Babyak, M.; Keršys, R.; Neduzha, L. Improving the dependability evaluation technique of a transport vehicle. In Proceedings of the 24th International Scientific Conference Transport Means, Kaunas, Lithuania, 30 September–2 October 2020; pp. 646–651.
69. Lunys, O.; Neduzha, L.; Tatarinova, V. Stability research of the main-line locomotive movement. In Proceedings of the 23rd International Conference Transport Means, Palanga, Lithuania, 2–4 October 2019; pp. 1341–1345.
70. Bondarenko, I.; Lunys, O.; Neduzha, L.; Keršys, R. Dynamic track irregularities modeling when studying rolling stock dynamics. In Proceedings of the 23rd International Scientific Conference Transport Means, Palanga, Lithuania, 2–4 October 2019; pp. 1014–1019.
71. Kalivoda, J.; Neduzha, L. Running Dynamics of Rail Vehicles. *Energies* **2022**, *15*, 5843. [CrossRef]
72. Klimenko, I.; Kalivoda, J.; Neduzha, L. Influence of Parameters of Electric Locomotive on its Critical Speed. In *Lecture Notes in Intelligent Transportation and Infrastructure, Proceedings of the TRANSBALTICA XI: Transportation Science and Technology, Vilnius, Lithuania, 2–3 May 2019*; Gopalakrishnan, K., Prentkovskis, O., Jackiva, I., Junevičius, R., Eds.; Springer: Cham, Switzerland, 2020; pp. 531–540. [CrossRef]
73. Bondarenko, I.; Campisi, T.; Tesoriere, G.; Neduzha, L. Using Detailing Concept to Assess Railway Functional Safety. *Sustainability* **2023**, *15*, 18. [CrossRef]
74. Myamlin, S.; Dailidka, S.; Neduzha, L. Mathematical modeling of a cargo locomotive. In Proceedings of the 16th International Conferenceon Transport Means, Kaunas, Lithuania, 25–26 October 2012; pp. 310–312.
75. Zelenko, Y.; Zelenko, D.; Neduzha, L. Contemporary principles for solving the problem in noise reduction from railway rolling stock. In *IOP Conference Series: Materials Science and Engineering*; IOP Publishing: Bristol, UK, 2020; Volume 985, p. 012015. [CrossRef]
76. Czupryński, A. Comparison of Properties of Hardfaced Layers Made by a Metal-Core-Covered Tubular Electrode with a Special Chemical Composition. *Materials* **2020**, *13*, 5445. [CrossRef] [PubMed]
77. Zheng, B.; Yu, S.; Yu, Z.; Tang, L. The preparation method and application of aluminum alloy flux-cored wire for wire arc additive manufacturing. *Weld. World* **2025**, *70*, 407–426. [CrossRef]
78. Makarenko, N.A.; Nevidomskij, V.A. Thermal cycles in plasma MIG surfacing. *Avtomat. Svarka* **2003**, *1*, 45–47.
79. Krbata, M.; Kohutiar, M.; Escherova, J.; Klučiar, P.; Studeny, Z.; Trembach, B.; Beronská, N.; Breznická, A.; Timárová, Ľ. Continuous Cooling Transformation of Tool Steels X153CrMoV12 and 100MnCrW4: Analysis of Microstructure and Hardness Changes. *Appl. Mech.* **2025**, *6*, 16. [CrossRef]
80. Rust, B.; Schmidt, J.; Stroetmann, R. Influence of the cooling time $t_{8/5}$ on weld metals. *Weld. World* **2025**, *69*, 2961–2974. [CrossRef]
81. Orečny, M.; Buršak, M.; Viňaš, J. The influence of heat treatment on the abrasive wear resistance of a construction and a tool steel. *Metalurgija* **2015**, *54*, 91–193.
82. Prysyazhnyuk, P.; Shlapak, L.; Semyanyk, I.; Kotsyubynsky, V.; Troshchuk, L.; Korniy, S.; Artym, V. Analysis of the effects of alloying with Si and Cr on the properties of manganese austenite based on ab initio modelling. *East.-Eur. J. Enterp. Technol.* **2020**, *6*, 28–36. [CrossRef]
83. Fagundes, J.G.; Moreno, A.M.; Ribeiro, P.H.; Arias, A.R.; Bracarense, A.Q. Formation of TiC by the application of Ti6Al4V machining chips as flux compounds of tubular wires. *J. Phys. Conf. Ser.* **2018**, *1126*, 012027. [CrossRef]
84. Fagundes Júnior, J.G.; Cardoso, A.H.C.; Bracarense, A.Q. Addition of TiO_2, $CaCO_3$ and CaF_2 as a flux of tubular wire applied for TiC in-situ reaction. *Soldag. Inspeção* **2020**, *25*, e2511. [CrossRef]
85. Prysyazhnyuk, P.; Yaremiy, I.P.; Kharlov, A.H.; Makohin, M.P.; Umantsiv, I.M.; Savchyn, V.V.; Misiuk, O.I. First-Principles Study of the Mechanical Properties of (Ti,V)C Solid Solutions. *Phys. Chem. Solid. State* **2025**, *26*, 377–385. [CrossRef]
86. Bartkowski, D.; Bartkowska, A.; Olszewska, J.; Przestacki, D.; Ulbrich, D. Stellite-6/(WC+TiC) Composite Coatings Produced by Laser Alloying on S355 Steel. *Materials* **2023**, *16*, 5000. [CrossRef] [PubMed]
87. Sukhova, O.V. Formation of structure and properties of boron-rich Fe–B–C alloys alloyed with Cr, V, Nb or/and mo. *Metallofiz. Noveish. Tekhnol.* **2021**, *43*, 355–365. [CrossRef]
88. Ivanov, O.O.; Prysyazhnyuk, P.M.; Marynenko, S.Y.; Bodrova, L.G.; Kramar, G.M.; Koval, I.V. Thermodynamic Modeling of the Phase Composition of Fe–Me–C–B System Coatings Materials to Increase Crack Resistance, Hardness, and Wear Resistance. *Strength Mater.* **2025**, *57*, 304–311. [CrossRef]
89. Efremenko, V.G.; Chabak, Y.G.; Shimizu, K.; Golinskyi, M.A.; Lekatou, A.G.; Petryshynets, I.; Efremenko, B.V.; Halfa, H.; Kusumoto, K.; Zurnadzhy, V.I. The novel hybrid concept on designing advanced multi-component cast irons: Effect of boron and titanium (Thermodynamic modelling, microstructure and mechanical property evaluation). *Mater. Charact.* **2023**, *197*, 112691. [CrossRef]

90. Erokhin, A.A.; Zelenova, V.I.; Ioffe, I.S. Zavisimost' reakcij mezhdu metallom i shihtoj serdechnika ot harakteristik poroshkovoj provoloki i rezhima svarki [Dependence of reactions between metal and core flux on the characteristics of flux-cored wire and welding mode]. *Avtomat. Svarka* **1978**, *7*, 18–21.
91. Trembach, B.O.; Silchenko, Y.A.; Sukov, M.G.; Ratska, N.B.; Duriagina, Z.A.; Krasnoshapka, I.V.; Kabatskyi, O.V.; Rebrova, O.M. Development of a Model of Transition Element Factor of Alloying Elements of Self-Shielding Flux-Cored Powder Wire and Optimization of Its Core Filler Composition. *Mater. Sci.* **2024**, *59*, 733–740. [CrossRef]
92. Trembach, B.; Grin, A.; Makarenko, N.; Zharikov, S.; Trembach, I.; Markov, O. Influence of the core filler composition on the recovery of alloying elements during the self-shielded flux-cored arc welding. *J. Mater. Res. Technol.* **2020**, *9*, 10520–10528. [CrossRef]
93. Coetsee, T.; De Bruin, F. Investigation of Copper as Collector Metal in Sodium-Oxide Fluxed Aluminothermic Reduction of Manganese Ore. *Crystals* **2026**, *16*, 50. [CrossRef]
94. Gucwa, M.; Winczek, J.; Bęczkowski, R.; Dośpiał, M. Structure and properties of coatings made with self shielded cored wire. *Arch. Metall. Mater.* **2016**, *16*, 39–42. [CrossRef]
95. Yuzvenko, Y.A.; Kyryliuk, G.A.; Krivchikov, S.Y. Model of melting of self-shielding flux-cored wire. *Avtomat. Svarka* **1983**, *1*, 26–28.
96. Yamamoto, E.; Yamazaki, K.; Suzuki, K.F. Koshiishi Effect of Flux Ratio in Flux-Cored Wire on Wire Melting Behaviour and Fume Emission Rate. *Weld World* **2010**, *54*, R154–R159. [CrossRef]
97. Trinh, N.Q.; Le, D.K.; Tashiro, S.; Bui, H.V.; Tanaka, T. Optimization of metal transfer in rutile flux-cored arc welding through controlled CO_2 concentration in argon–CO_2 shielding gas. *J. Manuf. Process.* **2024**, *124*, 590–603. [CrossRef]
98. Le, D.K.; Tashiro, S.; Trinh, N.Q.; Tanaka, T.; Bui, H.V. Elucidation of alkali element's role in optimizing metal transfer behavior in rutile-type flux-cored arc welding. *J. Manuf. Process.* **2025**, *139*, 105–125. [CrossRef]
99. Trembach, I.O.; Trembach, B.O.; Grin, A.G.; Luzhetskyy, R.Y.; Brechko, V.O.; Zakovorotniy, O.Y.; Balenko, O.I.; Molchanov, H.I.; Rebrova, O.M.; Kabatskyi, O.V. Application of a complete factorial experiment for optimization of the filling factor and charge density of self-shielding flux-cored powder wire. *Mater. Sci.* **2025**, *60*, 445–452. [CrossRef]
100. Trembach, B.O.; Hlushkova, D.V.; Hvozdetskyi, V.M.; Vynar, V.A.; Zakiev, V.I.; Kabatskyi, O.V.; Savenok, D.V.; Zakavorotnyi, O.Y. Prediction of Fill Factor and Charge Density of Self-Shielding Flux-Cored Wire with Variable Composition. *Mater. Sci.* **2023**, *59*, 18–25. [CrossRef]
101. Trinh, N.Q.; Tashiro, S.; Suga, T.; Kakizaki, T.; Yamazaki, K.; Morimoto, T.; Shimizu, H.; Lersvanichkool, A.; Bui, H.V.; Tanaka, M. Effect of Flux Ratio on Droplet TransferBehavior in Metal-Cored Arc Welding. *Metals* **2022**, *12*, 1069. [CrossRef]
102. Zhudra, A.P.; Krivchikov, S.Y.; Petrov, V.V. Vliyanie grafita na kinetiku perekhoda ugleroda v svarochnuyu vannu pri naplavke poroshkovoy provolokoy [Influence of graphite on the kinetics of carbon transfer into the weld pool during flux-cored wire surfacing]. *Avtomat. Svarka* **2006**, *11*, 32–35.
103. de Resende, A.A.; Duarte, C.A.R. The role of sustainability in the welding process: Context, technologies and challenges. *Environ. Dev. Sustain.* **2025**. [CrossRef]
104. Trembach, B.; Balenko, O.; Davydov, V.; Brechko, V.; Trembach, I.; Kabatskyi, O. Prediction the Melting Characteristics of Self-Shielded Flux Cored arc Welding (FCAW-S) with Exothermic Addition (CuO-Al). In Proceedings of the IEEE 4th International Conference on Modern Electrical and Energy System (MEES), Kremenchuk, Ukraine, 20–23 October 2022; pp. 1–6. [CrossRef]
105. Wang, J.; Li, H.; Hu, C.; Wang, Z.; Han, K.; Liu, D.; Wang, J.; Zhu, Q. The Efficiency of Thermite-Assisted Underwater Wet Flux-Cored Arc Welding Process: Electrical Dependence, Microstructural Changes, and Mechanical Properties. *Metals* **2023**, *13*, 831. [CrossRef]
106. Trembach, B.; Silchenko, Y.; Balenko, O.; Hlachev, D.; Kulahin, K.; Heiko, H.; Bellorin-Herrera, O.; Khabosha, S.; Zakovorotnyi, O.; Trembach, I. Study of the hardfacing process using self-shielding flux-cored wire with an exothermic addition with a combined oxidizer of the Al-(CuO/Fe_2O_3) system. *Int. J. Adv. Manuf. Technol.* **2024**, *134*, 309–335. [CrossRef]
107. Li, H.L.; Liu, D.; Guo, N.; Chena, H.; Dua, Y.P.; Feng, J.C. The effect of alumino-thermic addition on underwater wet welding process stability. *J. Mater. Process. Technol.* **2017**, *245*, 149–156. [CrossRef]
108. Trembach, B.; Trembach, I.; Grin, A.; Makarenko, N.; Babych, O.; Knyazev, S.; Musairova, Y.; Krbata, M.; Balenko, O.; Vorobiov, O.; et al. Study of the Effects of Hardfacing Modes Carried out by FCAW-S with Exothermic Addition of MnO_2-Al on Non-Metallic Inclusions, Grain Size, Microstructure and Mechanical Properties. *Eng* **2025**, *6*, 125. [CrossRef]
109. Trembach, B.; Grin, A.; Subbotina, V.; Vynar, V.; Knyazev, S.; Zakiev, V.; Kabatskyi, O. Effect of Exothermic Addition (CuO-Al) on the Structure, Mechanical Properties and Abrasive Wear Resistance of the Deposited Metal During Self-Shielded Flux-Cored Arc Welding. *Tribol. Ind.* **2021**, *43*, 452–464. [CrossRef]
110. Trembach, B.; Trembach, I.; Grin, A.; Makarenko, N.; Rebrov, O.; Musairova, Y.; Kuravska, N.; Knyazev, S.; Krasnoshapka, I.; Kuravskyi, M.; et al. Optimisation of hardfacing conditions carried out by self-shielded flux-cored wire using combined Taguchi method and factorial design. *Int. J. Adv. Manuf. Technol.* **2025**, *140*, 1367–1408. [CrossRef]
111. Li, H.; Hu, C.; Hu, J.; Han, K.; Wang, Z.; Yang, R.; Liu, D. Underwater wet welding of high-strength low-alloy steel using self-shielded flux-cored wire with highly exothermic Al/CuO mixture. *J. Mater. Process. Technol.* **2024**, *328*, 118404. [CrossRef]

112. Trembach, B.; Trembach, I.; Maliuha, V.; Knyazev, S.; Krbata, M.; Kabatskyi, O.; Balenko, O.; Zarichniak, Y.; Brechka, M.; Mykhailo, B.; et al. Study of self-shielded flux-cored wire with exothermic additions CuO-Al on weld bead morphology, microstructure, and mechanical properties. *Int. J. Adv. Manuf. Technol.* **2025**, *137*, 4685–4711. [CrossRef]
113. Assunção, M.T.; Bracarense, A.Q. A novel strategy to improve melting efficiency and arc stability in underwater FCAW via contact tip air chamber. *J. Manuf. Process.* **2023**, *104*, 1–16. [CrossRef]
114. Lozynskyi, V.; Trembach, B.; Katinas, E.; Sadovyi, K.; Krbata, M.; Balenko, O.; Krasnoshapka, I.; Rebrova, O.; Knyazev, S.; Kabatskyi, O.; et al. Effect of Exothermic Additions in Core Filler on Arc Stability and Microstructure during Self-Shielded, Flux-Cored Arc Welding. *Crystals* **2024**, *14*, 335. [CrossRef]
115. Trembach, B.; Dmitriiev, O.; Kulahin, K.; Balenko, O.; Maliuha, V.; Neduzha, L. Hybrid Optimization of Hardfacing Conditions and the Content of Exothermic Additions in the Core Filler During the Flux-Cored Arc Welding Process. *Eng* **2026**, *7*, 23. [CrossRef]
116. Laganà, F.; Pratticò, D.; Quattrone, M.F.; Pullano, S.A.; Calcagno, S. Hybrid AI–Taguchi–ANOVA Approach for Thermographic Monitoring of Electronic Devices. *Eng* **2026**, *7*, 28. [CrossRef]
117. Aita, C.A.G.; Goss, I.C.; Rosendo, T.S.; Tier, M.D.; Wiedenhoft, A.; Reguly, A. Shear strength optimization for FSSWAA6060-T5 joints by Taguchi and full factorial design. *J. Mater. Res. Technol.* **2020**, *9*, 16072–16079. [CrossRef]
118. Alao, A.R. Simultaneous optimization of multivariate surface roughness parameters in precision grinding of silicon by unsupervised machine learning. *Int. J. Adv. Manuf. Technol.* **2025**, *139*, 3543–3553. [CrossRef]
119. Pratiwi, D.K.; Arifin, A.; Gunawan; Mardhi, A.; Afriansyah. Investigation of Welding Parameters of Dissimilar Weld of SS316 and ASTM A36 Joint Using a Grey-Based Taguchi Optimization Approach. *J. Manuf. Mater. Process.* **2023**, *7*, 39. [CrossRef]
120. Thekkuden, D.T.; Sherif, M.M.; Alkhedher, M.; Iftikhar, S.H.; Mourad, A.H.I. Integrated Taguchi-PCA-GRA based multi objective optimization of tube projection and radial clearance for friction stir welded heat exchanger tube-to-tube sheet joints. *Int. J. Lightweight Mater. Manuf.* **2024**, *7*, 914–924. [CrossRef]
121. Arpitha, B.; Parthasarathy, P. Enhanced approach for geopolymer mix-design and performance evaluation: Integrating hybrid Taguchi-GRA-PCA for improved properties and behavioral insights. *Constr. Build. Mater.* **2024**, *433*, 136701. [CrossRef]
122. Tomita, R.K.; Park, S.W. Analysis of activated sludge process using multivariate statistical tools—A PCA approach. *Chem. Eng. J.* **2002**, *90*, 283–290. [CrossRef]
123. Shahapurkar, K.; Chenrayan, V.; Soudagar, M.E.M.; Badruddin, I.A.; Shahapurkar, P.; Elfasakhany, A.; Mujtaba, M.; Siddiqui, M.I.H.; Ali, M.A.; Mahlia, T.M.I. Leverage of Environmental Pollutant Crump Rubber on the Dry Sliding Wear Response of Epoxy Composites. *Polymers* **2021**, *13*, 2894. [CrossRef]
124. Kassov, V.; Berezshna, O.; Yermakova, S.; Turchanin, D.; Malyhina, S. Features of heating and melting of powder tape for surfacing of composite and complex-alloyed alloys. *East.-Eur. J. Enterp. Technol.* **2025**, *2*, 60–67. [CrossRef]
125. Zuo, X.; Lv, Z.; Wang, Y.; Chen, X.; Qi, W. Microstructural Organization and Mechanical Properties of 5356 Aluminum Alloy Wire Arc Additive Manufacturing Under Low Heat Input Conditions. *Metals* **2025**, *15*, 116. [CrossRef]
126. Lee, S.; Na, H.; Kim, B.; Kim, D.; Kang, C. Effect of Niobium on the Ferrite Continuous-Cooling-Transformation (CCT) Curve of Ultrahigh-Thickness Cr-Mo Steel. *Metall. Mater. Trans. A* **2013**, *44*, 2523–2532. [CrossRef]
127. Maruyama, N.; Sugiyama, M.; Hara, T.; Tamehiro, H. Precipitation and phase transformation of copper particles in low alloy ferritic and martensitic steels. *Mater. Trans. JIM* **1999**, *40*, 268–277. [CrossRef]
128. Jiao, Z.B.; Luan, J.H.; Zhang, Z.W.; Miller, M.K.; Ma, W.B.; Liu, C.T. Synergistic effects of Cu and Ni on nanoscale precipitation and mechanical properties of high-strength steels. *Acta Mater.* **2013**, *61*, 5996–6005. [CrossRef]
129. Hou, Q.; He, Y.; Gao, J. Microstructure and properties of Fe–C–Cr–Cu coating deposited by plasma transferred arc process. *Surf. Coat. Technol.* **2006**, *201*, 3685–3690. [CrossRef]
130. Yi, Y.; Xing, J.; Wan, M.; Yu, L.; Lu, Y.; Jian, Y. Effect of Cu on Microstructure, Crystallography and Mechanical Properties in Fe-B-C-Cu Alloys. *Mater. Sci. Eng. A* **2017**, *708*, 274–284. [CrossRef]
131. Ohtsuka, H.; Ghosh, G.; Nagai, K. Effects of Cu on diffusional transformation behavior and microstructure in Fe-Mn-Si-C steels. *ISIJ Int.* **1997**, *37*, 296–301. [CrossRef]
132. Babu, S.S. Thermodynamic and Kinetic Models for Describing Microstructure Evolution during Joining of Metals and Alloys. *Int. Mater. Rev.* **2009**, *54*, 333–367. [CrossRef]
133. Mishra, S.; Chhibber, R.; Singla, Y.K. Effects of CaO–ZrO_2–SiO_2–CaF_2–TiO_2-based electrode coating components on weld chemistry and microhardness. *J. Mater. Res. Technol.* **2024**, *33*, 8918–8928. [CrossRef]
134. Chai, C.S.; Eagar, T.W. Slag metal reactions in binary CaF_2-Metal Oxide welding fluxes. *Weld J.* **1982**, *61*, 229–232.
135. Tuliani, S.S.; Boniszewski, T.; Eaton, N.F. Notch toughness of commercial submerged arc weld metal. *Weld. Met. Fabr.* **1969**, *37*, 327–339.
136. Coetsee, T.; De Bruin, F. Insight into the Chemical Behaviour of Chromium in CaF_2-SiO_2-Al_2O_3-MgO Flux Applied in Aluminium-Assisted Alloying of Carbon Steel in Submerged Arc Welding. *Minerals* **2022**, *12*, 1397. [CrossRef]

137. Bang, K.S.; Park, C.; Jung, H.C.; Lee, J.B. Effects of flux composition on the element transfer and mechanical properties of weld metal in submerged arc welding. *Met. Mater. Int.* **2009**, *15*, 471–477. [CrossRef]
138. Mahajan, S.; Kumar, J.; Chhibber, R. High-Temperature Wettability Investigations on Laboratory-Developed CaO-CaF_2-SiO_2-Al_2O_3 Flux System-Based Welding Electrode Coatings for Power Plant Applications. *Silicon* **2020**, *12*, 2741–2753. [CrossRef]
139. Shlepakov, V.N.; Kotelchuk, A.S.; Naumeiko, S.M. Features of interaction of molten metal with gases in self-shielded flux-cored wire welding. *Paton Weld. J.* **2000**, *5*, 10–14.
140. Trembach, B.O.; Grin, A.G.; Miloserdov, P.A.; Trembach, I.O. Thermodynamic studies of CuO-Fe_2O_3-Al exotermic mixture with a combine oxidant in self-shielding flux cored wires. *Her. Donbass State Eng. Acad.* **2019**, *2*, 41–46. [CrossRef]
141. Garg, J.; Garg, S.B.; Singh, K.; Selvaraj, S. Influence of recycled SAW slag and process parameters on the composition of stainless steel claddings. *J. Adhes. Sci. Technol.* **2025**, *39*, 1720–1736. [CrossRef]
142. Liu, Z.; Li, Y.X.; Chen, X.; Hu, K.H. Microstructure and mechanical properties of high boron white cast iron. *Mater. Sci. Eng. A* **2008**, *486*, 112–116. [CrossRef]
143. Rajičić, B.; Maslarević, A.; Bakić, G.; Maksimović, V.; Đukić, M.B. Erosion behaviour of Fe-Cr-C alloys: Cast alloy versus coating. *Tribol. Mater.* **2024**, *3*, 59–66. [CrossRef]
144. Su, L.; Ji, X.; Zhao, L.; Zhai, W.; Xu, L.; Dong, H.; Liu, Y.; Peng, J. First principles investigation of binary chromium carbides Cr7C3, Cr3C2 and Cr23C6: Electronic structures, mechanical properties and thermodynamic properties under pressure. *Materials* **2022**, *15*, 558. [CrossRef]
145. Babinets, A.A.; Voron, M.M.; Schwab, S.L. Influence of the granulometric composition of flux-cored wire on the surfacing stability and structure of 50Kh2N2MFS metal. *Mater. Sci.* **2026**, *61*. [CrossRef]
146. Kassov, V.D. Computer calculation of the composition of a self-shielding flux-cored wire for vibroarc surfacing. *Weld. Int.* **1991**, *5*, 738–740. [CrossRef]
147. Ryabtsev, I.O.; Babinets, A.A.; Lentugov, I.P.; Zhdanov, V.O.; Ryabtsev, I.I.; Osin, V.V. Methods of Investigation of the Deposited Metal Properties and Their Application for the Development of Flux Cored Wires. *Mater. Sci.* **2023**, *59*, 467–473. [CrossRef]
148. Ryabtsev, I.O.; Babinets, A.A.; Lentyuhov, I.P. Control of the formation of metal structure surface with flux-cored wires. *Mater. Sci.* **2024**, *60*, 298–305. [CrossRef]
149. Arneitz, S.; Minkowitz, L.; Griffond, A.; de Rango, P.; Rivoirard, S.; Sommitsch, C. Influence of key printing parameters on the development of microstructure and texture in Fe–Cr–Co and its effects on the magnetic properties. *Prog. Addit. Manuf.* **2026**. [CrossRef]
150. Arneitz, S.; Bin Ali, W.; Adachi, S.; Horii, S.; Sommitsch, C. Additive manufacturing of Fe–Cr–Co magnet structures with a functionally graded chemical composition. *Prog. Addit. Manuf.* **2026**, *11*, 1187–1201. [CrossRef]
151. Kowalczyk, J.; Jósko, M.; Wieczorek, D.; Sędłak, K.; Nowak, M. The Influence of the Hardness of the Tested Material and the Surface Preparation Method on the Results of Ultrasonic Testing. *Appl. Sci.* **2023**, *13*, 9904. [CrossRef]
152. Grochalski, K.; Kowalczyk, J.; Jósko, M.; Wieczorowski, M. Evaluation of the Influence of Surface Roughness Parameters on Ultrasonic Rayleigh Waveforms. *Materials* **2024**, *17*, 5493. [CrossRef]
153. Sekmen, K.; Rehbein, T.; Johlitz, M.; Lion, A.; Constantinescu, A. Material modelling of the photopolymers for additive manufacturing processes. In Proceedings of the 33rd Annual International Solid Freeform Fabrication Symposium—An Additive Manufacturing Conference, Austin, TX, USA, 25–27 July 2022; pp. 94–106.
154. Gurauskis, D.; Kasparaitis, A.; Sokolovskij, E.; Matijošius, J.; Kilikevičius, A. Analysis of Stainless-Steel Tape Dynamic Behavior and Its Impact on Raster Scale Formation Accuracy. *Machines* **2025**, *13*, 124. [CrossRef]
155. Caliendo, C.; Russo, I.; Genovese, G. Evaluation of Passenger Train Safety in the Event of a Liquid Hydrogen Release from a Freight Train in a Tunnel Along an Italian High-Speed/High-Capacity Rail Line. *Appl. Sci.* **2025**, *15*, 10660. [CrossRef]
156. Granzner, M.; Strauss, A.; Reiterer, M.; Cao, M.; Novák, D. Data-Driven Condition Assessment and Life Cycle Analysis Methods for Dynamically and Fatigue-Loaded Railway Infrastructure Components. *Infrastructures* **2023**, *8*, 162. [CrossRef]